Bioactive Materials 35 (2024) 346–361

Contents lists available at ScienceDirect

Bioactive Materials

journal homepage: www.keaipublishing.com/en/journals/bioactive-materials

Piezoelectric hydrogel for treatment of periodontitis through bioenergetic activation

Xin Liu [a,*,1], Xingyi Wan [b,c,1], Baiyan Sui [a,1], Quanhong Hu [b], Zhirong Liu [b,c], Tingting Ding [a], Jiao Zhao [a], Yuxiao Chen [a], Zhong Lin Wang [b,c,**], Linlin Li [b,c,***]

[a] Department of Dental Materials, Shanghai Biomaterials Research & Testing Center, Shanghai Ninth People's Hospital, Shanghai Jiao Tong University School of Medicine, College of Stomatology, Shanghai Jiao Tong University, National Center for Stomatology, National Clinical Research Center for Oral Diseases, Shanghai Key Laboratory of Stomatology, Shanghai, 200011, PR China

[b] Beijing Institute of Nanoenergy and Nanosystems, Chinese Academy of Sciences, Beijing, 101400, PR China

[c] School of Nanoscience and Technology, University of Chinese Academy of Sciences, Beijing, 100049, PR China

ARTICLE INFO

Keywords:
Piezoelectric hydrogel
Mitochondrial bioenergetics
Periodontitis
Bone regeneration
Macrophage polarization

ABSTRACT

The impaired differentiation ability of resident cells and disordered immune microenvironment in periodontitis pose a huge challenge for bone regeneration. Herein, we construct a piezoelectric hydrogel to rescue the impaired osteogenic capability and rebuild the regenerative immune microenvironment through bioenergetic activation. Under local mechanical stress, the piezoelectric hydrogel generated piezopotential that initiates osteogenic differentiation of inflammatory periodontal ligament stem cells (PDLSCs) via modulating energy metabolism and promoting adenosine triphosphate (ATP) synthesis. Moreover, it also reshapes an anti-inflammatory and pro-regenerative niche through switching M1 macrophages to the M2 phenotype. The synergy of tilapia gelatin and piezoelectric stimulation enhances in situ regeneration in periodontal inflammatory defects of rats. These findings pave a new pathway for treating periodontitis and other immune-related bone defects through piezoelectric stimulation-enabled energy metabolism modulation and immunomodulation.

1. Introduction

Periodontitis affects up to 50% of the global population and has a significant impact on quality of life, causing serious alveolar bone defects, tooth loss, mastication dysfunction, and poor esthetics [1,2]. The natural self-repairing potential of alveolar bone in periodontitis is severely compromised due to the imbalance of pro- and anti-inflammatory macrophages and excessive cytokine excretion, which hampers cellular bioenergetics and differentiation capacity of resident stem cells [3–8]. In the periodontal ligament of periodontitis, stem cells exhibit serious mitochondrial dysfunction with decreased ATP production [6–9]. Thus, energy metabolism plays a dominant role in stem cell differentiation and macrophage polarization, both of which are essential for bone regeneration [10–13].

Recently, activation of energy metabolic status has been taken into consideration during designing biomaterial scaffolds for bone regeneration. Researchers found that the biomaterials capable of releasing inherent metabolic regulators or providing intrinsic physicochemical cues can modulate the energy metabolism of stem cells [14–17]. However, developing efficient strategies and biomaterials with the capability of activating the bioenergetics of impaired stem cells in inflammation-related pathologies remains a huge challenge.

Electrical stimulation (ES) has been clinically proven to be beneficial for stimulating osteogenesis and angiogenesis, alleviating inflammatory response and tuning macrophage polarization through improving mitochondrial function and inducing more ATP synthesis [18–20]. However, conventional electrical stimulation requires bulk devices, wired connections, and invasive and implantable electrodes [21,22]. As alveolar bone is periodically stress-bearing tissue, piezoelectric transducers offer a new solution to the dilemma [23–25]. Compared to

Peer review under responsibility of KeAi Communications Co., Ltd.

* Corresponding author.
** Corresponding author.
*** Corresponding author.
E-mail addresses: liuxin8253@sjtu.edu.cn (X. Liu), zhong.wang@mse.gatech.edu (Z.L. Wang), lilinlin@binn.cas.cn (L. Li).
[1] The authors contributed equally to this work.

https://doi.org/10.1016/j.bioactmat.2024.02.011
Received 28 July 2023; Received in revised form 26 January 2024; Accepted 7 February 2024
2452-199X/© 2024 The Authors. Publishing services by Elsevier B.V. on behalf of KeAi Communications Co. Ltd. This is an open access article under the CC BY-NC-ND license (http://creativecommons.org/licenses/by-nc-nd/4.0/).

conventional ES, piezoelectric stimulation presents unique advantages such as non-invasiveness, wireless manipulation, self-powered energy supply, and high spatiotemporal precision. Despite much attention has been paid to piezoelectricity-stimulated tissue regeneration (e.g., nerve, bone, periodontal tissues) [23–27], its capacity to simultaneously activate the bioenergetics of stem cells and modulate the immune microenvironment is overlooked [28,29].

In this work, inspired by the phenomenon that electrical stimulation can stimulate mitochondria to produce ATP, we develop a wireless piezoelectric stimulation system to activate bioenergetics for the regeneration of injured tissues in periodontitis. To achieve this, we construct a piezoelectric hydrogel made from piezoelectric tetragonal $BaTiO_3$ nanoparticles (t-BTO NPs) and tilapia fish gelatin hydrogel [30–32]. Under mechanical activation, the triggered piezoelectric potential can improve the mitochondria bioenergetic function of inflammatory periodontal ligament stem cells (PDLSCs) and rescued their osteogenic differentiation. Furthermore, the piezoelectric stimulation and intrinsic anti-inflammatory activity of tilapia fish gelatin collaboratively switch the macrophage polarity from proinflammatory M1 phenotype towards anti-inflammatory M2 phenotype for osteogenesis. As a result, we successfully achieve in situ tissue regeneration in the inflammatory periodontal bone defects of rats (Scheme 1).

2. Materials and methods

2.1. Synthesis and characterization of piezoelectric hydrogel

2.1.1. Synthesis of c-BTO NPs

Cubic $BaTiO_3$ NPs (c-BTO NPs) was synthesized through a solvothermal reaction based on a previous report with some modifications [33]. Raw materials used included barium hydroxide monohydrate ($Ba(OH)_2{\cdot}8H_2O$ (Ba-hydroxide), 98 %, Aladdin) and $Ti[O(CH_2)_3CH_3]_4$ (Ti-butoxide, 97 %, Macklin). Initially, 17.018 g (50 mM) of Ti-butoxide was added to 20 mL of ethanol followed by the addition of 7 mL of ammonium hydroxide solution ($NH_3{\cdot}H_2O$, 25 %, Sinopharm Chemical Reagent Co). And 23.660 g (75 mM) of $Ba(OH)_2{\cdot}8H_2O$ was dissolved in 25 mL deionized (DI) water to obtain a clear solution. The resultant Ba-hydroxide solution was then added to the Ti precursor mixture under gentle stirring. The final suspension was transferred into a 100 mL Teflon-lined stainless-steel autoclave, heated at 200 °C for 48 h, and cooled down to room temperature. The product was washed repeatedly using DI water and high-purity ethanol, and dried at 80 °C for 24 h in a vacuum oven to obtain c-BTO NPs.

2.1.2. Synthesis of t-BTO NPs

A simple thermal calcination process was carried out to achieve the phase conversion of BTO NPs from cubic to tetragonal phase. In brief, the c-BTO NP powders were placed in a corundum crucible and heated at 90 °C for 4 h at a heating rate of 5 °C min^{-1}, followed by annealing under a heating rate for 2 °C min^{-1} at 800 °C for 4 h. The resultant powder of t-BTO NPs was naturally cooled to room temperature for further use.

2.1.3. Preparation of the piezoelectric hydrogel

Gelatin methacryloyl (GelMA) hydrogel was synthesized based on a previous report with some modifications [34]. 20 g of tilapia gelatin (Shanghai Fisheries Research Institute, China) was fully dissolved by adding 200 mL of PBS and stirring for 1 h at 50 °C. After passing nitrogen gas inside the chamber, 20 mL of methacrylic anhydride (MA, Sigma Aldrich, USA) was added dropwise at a rate of 0.5 mL min^{-1} under continuous stirring for 1 h. Subsequently, 800 mL of PBS was added to dilute the reaction mixture. The mixture was dialyzed with a 12–14 kDa dialysis membrane for 1 week to remove unreacted MA, and the product was freeze-dried to obtain GelMA. Proton nuclear magnetic resonance (^1H NMR) spectra were performed to verify MA grafting on gelatin using an NMR spectrometer (Varian Mercury-plus 400, Agilent Technologies, USA).

The BTO containing hydrogel was prepared by dispersing 0.05 % w/v t-BTO (or c-BTO), 10% w/v GelMA, and 0.25% w/v photoinitiator lithiumphenyl-2,4,6-trimethylbenzoylphosphinate (LAP) in a PBS solution. In brief, 20 mL PBS was added into a brown flask containing 0.05 g LAP powder to obtain 0.25% (w/v) LAP solution, subsequently, 2 g GelMA powder and 1 mg BTO NPs were added into 20 mL of 0.25% (w/v) LAP solution and then placed in an ultrasonic water bath. After ultrasonication for 15 min, the freshly prepared GelMA/BTO NPs solutions were cured under visible light (405 nm) for 30 s to obtain the piezoelectric hydrogel (GelMA + c-BTO or GelMA + t-BTO hydrogel).

2.1.4. Characterizations of c-BTO and t-BTO NPs

X-ray diffraction (XRD) spectra were measured using a D/MAX-TTRIII XRD system (Japan) with Cu Kα radiation (λ = 1.5406 Å, 2θ =

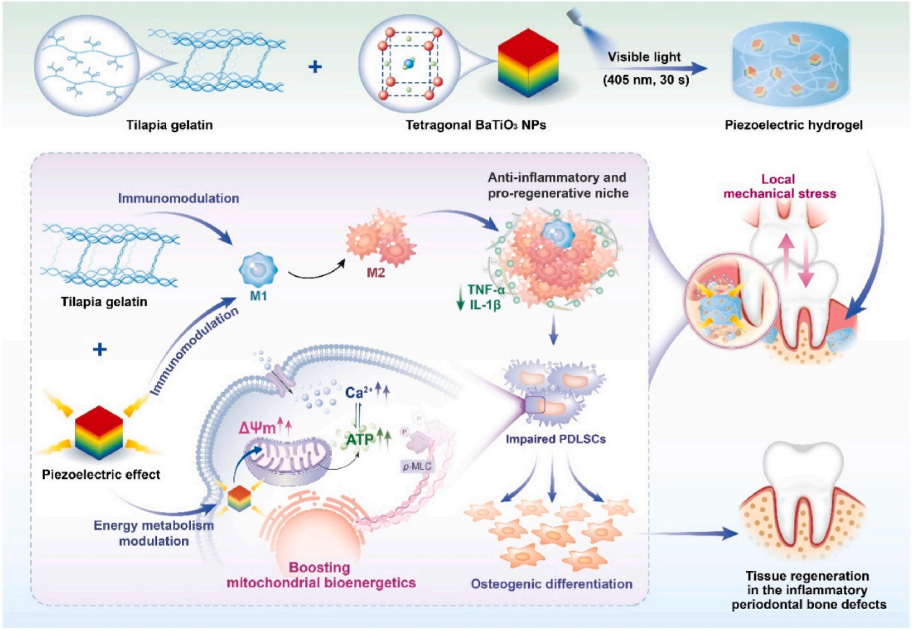

Scheme 1. Scheme illustrating the piezoelectric hydrogel for osteogenesis and immunomodulation in periodontitis through activation of bioenergetics.

10°–80°, 10 kV, 10 μA). Scanning electron microscopic (SEM) images were obtained using a field-emission S-4800 microscope (Hitachi, Japan). Transmission electron microscopic (TEM) photographs were recorded on a Tecnai G2 F20 high-resolution electron microscopy (FEI Company, US). Raman spectra were measured using a laser Raman spectrometer (LABRAM HR EVOLUTION, HORIBA JY, France) at an excitation wavelength of 532 nm. Hydrodynamic diameter and zeta potential were measured via dynamic light scattering (DLS) on the DelsaMax Pro instrument (Beckman Coulter Corporation, USA). Piezoresponse force microscopic (PFM) photographs and amplitude-butterfly loop of both c-BTO and t-BTO were measured using an atomic force microscope (MFP-3D, Asylum Research) with PFM mode under a contact mode with a conductive probe. Polarization-electric field hysteresis loops were tested using a ferroelectric tester (RTI-MultiFerroic, Radiant, USA).

2.1.5. Finite element modeling (FEM) simulation of t-BTO

The FEM simulation involves a three-dimensional analysis of a single t-BTO nanoparticle using the piezoelectric devices multiphysics interface method through COMSOL software [35]. This model consisted of a cubic-shaped t-BTO nanocrystal with a side length of 150 nm. The polarization was aligned along the global co-ordinate z-axis, and the center was fixed and grounded. Other material parameters used in the simulation, such as density (ρ), elasticity matrix (cE), coupling matrix (eES), and relative permittivity (ε_r) of t-BTO NPs, were provided as predefined materials parameters in COMSOL Multiphysics. The pressure force provided by ultrasound (frequency of 1 MHz and power density of 1 W cm^{-2}) was calculated to be 10^6 Pa. For comparison, the induced piezopotential distribution under different ultrasound power densities of 0.5, 1.5, and 2 W cm^{-2} was simulated in the same way.

2.1.6. Characterizations of the piezoelectric hydrogel

The morphology and elemental composition of the piezoelectric hydrogels were observed and analyzed using SEM-EDS mapping (Mira3, Czechia). The mechanical properties of the hydrogels were measured using universal material testing equipment. The mechanical loading force was carried out using a diameter of 6 mm and a height of 10 mm sample with a maximum compression strain of 80%. The compressive modulus of the samples was determined by dividing the stress by the strain in the linear portion of the stress-strain curve. To determine the piezoelectric properties of the hydrogels, we assembled the piezoelectric hydrogels into piezoelectric generators. Specifically, one side of a flexible Au electrode was affixed to the bottom of the mold. Next, the pre-polymer hydrogel solution was gently poured into the mold, and another layer of Au electrode was placed on the top of the solution. After the hydrogel was polymerized, piezoelectric generator was formed. The piezoelectric outputs were detected using a piezoelectric test system composed of universal digital meter (Keithley 6514, USA), a programmable linear motor linked with a computer. The generators were subjected to periodic compression generated by the self-controlled linear motor, and the corresponding voltage outputs under different pressures or ultrasound stimulation were recorded via a digital meter. To evaluate the release potential of nanoparticles in the cured samples, 100 μL of the cured sample was immersed in 1 mL PBS for 8 weeks at 37 °C. At 1, 2, 4, and 8 weeks, the solution was collected to determine Ba and Ti concentration using ICP-MS (Agilent 7700, USA).

2.2. In vitro study of PDLSCs

2.2.1. Optimizing t-BTO NPs concentrations and US power densities via cytotoxicity

PDLSCs were kindly gifted from Shanghai Stomatological Hospital in China and cultured in α-MEM medium (HyClone, USA) supplemented with 10% FBS, 1% penicillin and streptomycin (HyClone, USA) at 37 °C containing 5% CO_2. PDLSCs were cultured with t-BTO (50 μg mL^{-1} or 100 μg mL^{-1}) NPs in α-MEM medium. The outside of the bottom of the cell culture plate was applied with ultrasonic coupling agent (Shanghai Junkang Medical Equipment Co., China), and the ultrasound probe contacted the coupling agent and output to various ultrasound power densities (Variable parameters: 0, 0.2 W cm^{-2}, 0.4 W cm^{-2}, 0.6 W cm^{-2}, 0.8 W cm^{-2} and 1.0 W cm^{-2}. Fixed parameters: 1 MHz, 50% duty cycle, 60 s) to determine the safety concentration of t-BTO NPs and US power density that would not harm the cells. We used cytotoxicity as an indicator to select non-cytotoxic concentration of t-BTO (50 μg mL^{-1}) and ultrasound parameters (0.6 W cm^{-2}, 1 MHz, 50% duty cycle, 60 s) for subsequent experiments.

2.2.2. Treatment of PDLSCs and cell viability

PDLSCs were seeded at a density of 1×10^5 cells/well in 24-well plates and incubated for 24 h. Then 100 ng mL^{-1} of lipopolysaccharide (LPS) derived from periodontal pathogen was added to stimulate the cell for 24 h to obtain inflammatory PDLSCs (L-PDLSCs). These L-PDLSCs were then incubated with c-BTO (50 μg mL^{-1}) or t-BTO (50 μg mL^{-1}) NPs in α-MEM medium and exposed to US irradiation (US^+) or not (US^-). The cell treatments were divided into six groups: i) NC US^-, ii) c-BTO US^-, iii) t-BTO US^-, iv) NC US^+, v) c-BTO US^+, and vi) t-BTO US^+. Cell viability was measured using the MTS cell viability assay after 1, 3, and 5 days of additional culture.

2.2.3. Measurement of ATP level and mitochondrial membrane potential ($\Delta\psi_m$)

L-PDLSCs were treated as described above. The intracellular ATP level was detected using an enhanced ATP Assay Kit (Beyotime, China) and Cytation 3 Cell Imaging Multi-Mode Reader (Agilent Technologies, USA) after 3 days of additional incubation. $\Delta\psi_m$ was observed using 5,5′,6,6′-tetrachloro1,1′,3,3′-tetraethylimidazolium cyanide (JC-1) as a specific indicator (Beyotime, China).

2.2.4. Real-time quantitative PCR (qRT-PCR)

L-PDLSCs were treated with t-BTO US^+ and cultured for an additional 5 days. RNeasy Mini Kit (QiAGEN, Germany) was used to extract total RNA from the cells. The PrimeScriptTM RT reagent Kit (Takara, Japan) was used to generate complementary DNA (cDNA) from total RNA. The SYBR Premix EX Taq (Takara, Japan) and a detection system (Light cycler96, Roche, Switzerland) were used to perform qRT-PCR. The primer sequences are shown in Table S1.

2.2.5. ALP and alizarin red S staining

For ALP staining, L-PDLSCs were seeded in 24-well plates (3×10^4 cells/well), treated with t-BTO US^+ and cultured for an additional 14 days. ALP was stained with BCIP/NBT ALP kit (Beyotime, China) and observed under an inverted microscope (Leica, Germany). For alizarin red S (ARS) staining, L-PDLSCs were treated with t-BTO US^+ and cultured for an additional 21 days. The cells were stained with an ARS kit (GERMED, USA), and the red mineralized nodules images were captured. The ALP and ARS staining area ratio of the whole well was analyzed using Image-J.

2.2.6. RNA-sequencing and data processing.

The RNA level of L-PDLSCs in the NC US^- group and t-BTO US^+ group was extracted by TRIzol™ Reagent (ThermoFisher, USA). The cDNA library was created for data processing, the insertion fragments of cDNA libraries were detected using an Agilent 2100 Bioanalyzer, and the effective concentration of cDNA libraries was calculated using an ABI StepOnePlus Real-Time PCR System. Clean reads were mapped to the reference genome using HISAT after removing low-quality reads [36]. Clean reads were aligned to the reference gene sequence using Bowtie2 [37]. RSEM was used to quantify gene expression levels for each sample. Differential expression analysis was conducted using the R software (Padj<0.05, foldchange>2). TBTools was applied to generate the heat map illustrating gene expression levels [38].

2.2.7. Observation of intracellular localization

L-PDLSCs from various treatment groups were cultured for another 3 days. The L-PDLSCs of each group were collected, fixed, embedded and sectioned to observe the localization of NPs within the cells using TEM. Meanwhile, the Ba^{2+} content in BTO (c-BTO or t-BTO) treatment group of L-PDLSCs was measured using ICP-MS to assess the amount of NPs phagocytosed into the cells.

2.2.8. F-actin and p-MLC staining

L-PDLSCs after various treatments were cultured for an additional 3 days. After being fixed, permeabilized and blocked, the cells were incubated with *p*-MLC-2 monoclonal antibody (Cell Signaling Technology, USA) away from light at 4 °C overnight. Subsequently, the cells were incubated with anti-rabbit IgG secondary antibody (Abcam, UK), Alexa Fluor® 488-phalloidin (Beyotime, China), and 4′,6-diamidino-2-phenylindole (DAPI, Beyotime, China), respectively. Finally, the stained cells were observed using a laser scanning confocal microscope (LSCM, A1R, Nikon, Japan).

2.2.9. Intracellular calcium level

L-PDLSCs were incubated with 5 μM Fluo 4-AM (Invitrogen, USA) in the dark at 37 °C for 30 min, after which the supernatants were carefully removed. Intracellular fluorescence of L-PDLSCs was then recorded every 20 min for 24 h following various cell treatments.

2.3. In vitro study of RAW 264.7 cells

2.3.1. Cells culture and morphology observation

RAW 264.7 macrophages were obtained from the Chinese Academy of Sciences Cell Bank (Shanghai, China) and cultured in high-glucose DMEM (Hyclone, USA), supplemented with 10% FBS and 1% penicillin and streptomycin. For SEM observation, RAW 264.7 cells (1×10^5 cells/well) were seeded on a coverslip in 24-well plates for 24 h and stimulated with 100 ng mL^{-1} of LPS for 24 h, resulting in inflammatory RAW 264.7 referred to as L-RAW 264.7. L- RAW 264.7 cells were treated with BTO NPs with or without US, and cell morphology was observed using SEM (Mira3, Czechia). Additionally, cells were stained with Phalloidin (Beyotime, China) and DAPI (Beyotime, China) and examined using LSCM (A1R, Nikon, Japan).

2.3.2. Real time-PCR assay, RNA-sequencing and data processing

L-RAW 264.7 cells were treated with BTO and/or US and cultured for an additional 5 days. RNA extraction, acquisition of cDNA, and qRT-PCR assays and RNA-sequencing were performed. The primer sequences used are shown in Table S2.

2.4. In vivo study

2.4.1. Experimental design and animal surgical procedure

All the animal experiments were ethically reviewed and approved by the Independent Ethics Committee of Shanghai Ninth People's Hospital, Shanghai Jiao Tong University School of Medicine (Ethical number: SH9H-2022-A417-SB). Thirty-two male Sprague-Dawley rats (220–250 g) were divided into 4 groups: Blank control, GelMA, GelMA + c-BTO, and GelMA + t-BTO. All surgical procedures were performed under general anesthesia administered by intraperitoneal injection of 3% pentobarbital sodium. To construct an inflammatory periodontal defect, rats were injected with 10 μL of LPS (1 mg mL^{-1}) at the mediolateral aspect of the first left mandibular molar every three days during 30 days [39]. A 1-cm-long incision was then made on the left buccal surface of the rats to expose the mandible by separating the masticatory muscles and periosteum. A periodontal defect of approximately 5 × 2 × 2 mm was prepared using a low-speed dental handpiece, approximately 1 mm below the top of the alveolar ridge of the first molar. GelMA, GelMA + c-BTO, or GelMA + t-BTO were injected into the periodontal defect and light-cured for 30 s, respectively. The sham operation was set as a Blank group.

2.4.2. ELISA analysis of inflammatory factors

After 12 weeks of surgery, animals were stimulated by intraperitoneal injection of pilocarpine (10 mg/kg) under anesthesia, and stimulated saliva samples were collected by dropping them into a sterile plain bottle for a period of 10 min [40]. The concentrations of IL-1β, IL-6, and TNF-α in the saliva samples were detected using ELISA kits (Wellbio Biotechnology Co., Ltd, China) according to the manufacturer's protocols.

2.4.3. Micro-CT observation, H&E, immunohistochemistry and immunofluorescence staining

Mandible samples were collected at 4 and 12 weeks following the surgery and evaluated by micro-CT imaging, H&E staining, and immunofluorescence staining. Micro-CT (Skyscan 1076, Bruker, USA) was used to scan and analyze the mandible samples at 40 kV and 250 μA and the camera pixel size was set to 12.60 μm. CT-Analyzer (Bruker, USA) was used to reconstruct 3D images and analyze the quantitative data, including new bone volume (BV), bone volume/total volume fraction (BV/TV), and bone mineral density (BMD). Mandible samples were then decalcified in Ethylene Diamine Tetraacetic Acid (EDTA) solution and embedded in paraffin for H&E, immunohistochemistry (*p*-MLC), and immunofluorescence staining (Dapi-CD68-iNOS, and Dapi-CD68-CD206).

2.4.4. Observation of organ and hematological indicators

Hematology, blood biochemistry, and histopathological examinations of major organs were performed using the rats mentioned above.

2.4.5. Phenotype regulation of RAW 264.7 cells by the piezoelectric hydrogel

L-RAW 264.7 cells were incubated with GelMA (20 μL), GelMA + c-BTO (20 μL) or GelMA + t-BTO (20 μL) in a 24-well plate and exposed to US^+ or US^-. The cell treatments were divided into seven groups: i) NC US^-, ii) GelMA US^-, iii) GelMA + c-BTO US^-, iv) GelMA + t-BTO US^-, v) GelMA US^+, vi) GelMA + c-BTO US^+, and vii) GelMA + t-BTO US^+. After 5 days of these treatments, RNA extraction, acquisition of cDNA, and qRT-PCR assays of L-RAW 264.7 cells were performed.

2.4.6. Subcutaneous implantation assay in C57BL/6 mice

A total of fifteen C57BL/6 mice (18–20 g) were randomly divided into 3 groups (n = 5): Blank, GelMA, and GelMA + t-BTO. In brief, 20 μL of the cured sample was implanted subcutaneously in the back of the mouse. At 28 days postoperatively, spleens were collected for analysis of $CD4^+$ T cells, $CD8^+$ T cells, and $CD4^+/CD8^+$ ratio by flow cytometry.

2.5. Statistical analysis

The data are presented as mean ± standard deviation (S.D.). SPSS 20.0 software was used to conduct a statistical analysis of the data. The statistical comparisons were established using the one-way ANOVA or Student's t-test.

3. Results

3.1. Synthesis and characterization of piezoelectric hydrogel

We prepared the piezoelectric hydrogel by incorporating tetragonal phase piezoelectric $BaTiO_3$ NPs (t-BTO NPs) into a tilapia-derived gelatin methacryloyl (GelMA). Our previous study found that tilapia-derived GelMA had intrinsic anti-inflammatory activity [32], which can synergize the effect of piezoelectric stimulation [41]. We fabricated nonpiezoelectric cubic BTO NPs (c-BTO NPs) as a sham control. In the X-ray diffraction (XRD) pattern of t-BTO, the appearance of two split peaks located at $2\theta = 45°$ suggested the typical perovskite structure

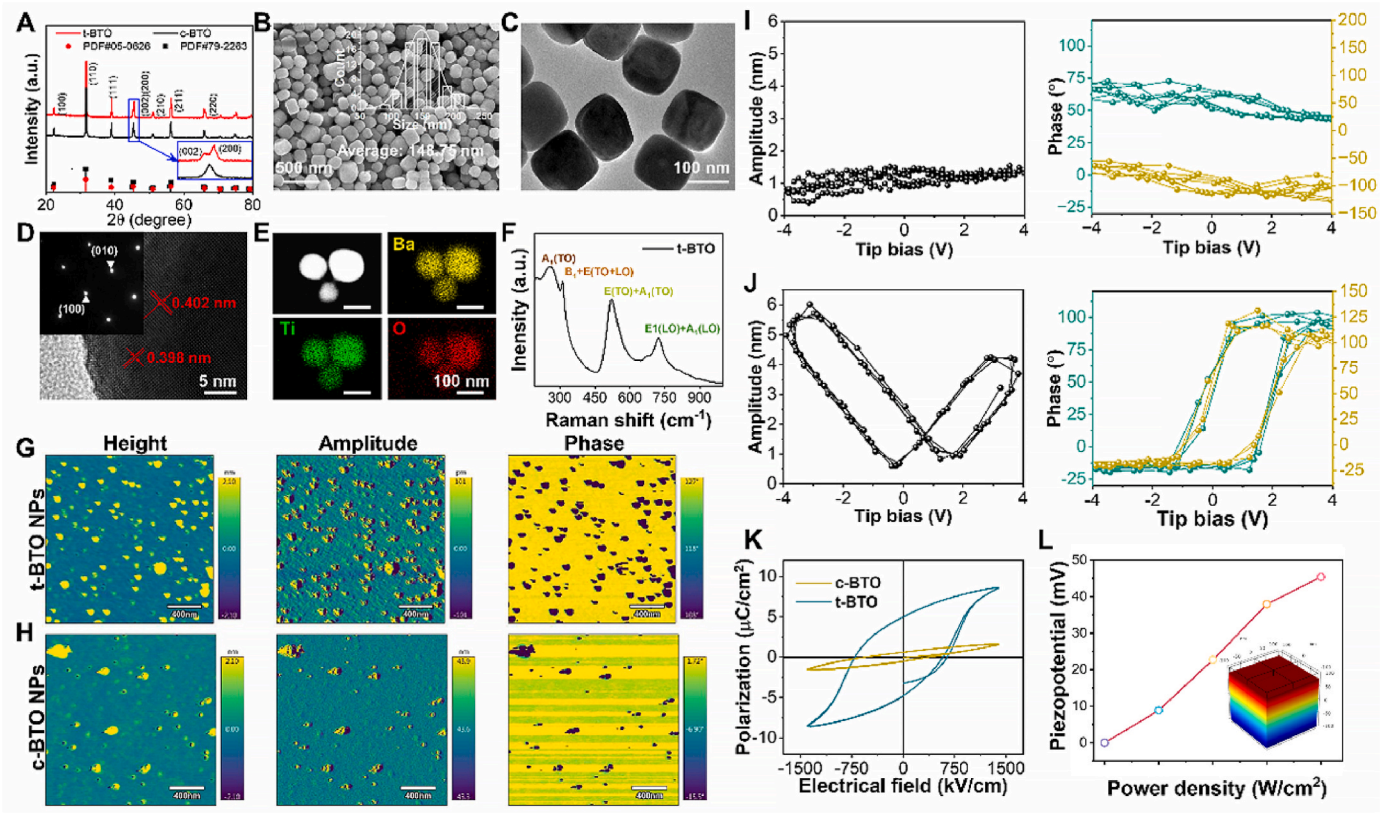

Fig. 1. Structural characterization and piezoelectric properties of BTO NPs. (A) XRD pattern of t-BTO NPs and the enlarged region in the red dot circle. (B) SEM image and the size distribution (inset) of t-BTO NPs. (C) TEM image of t-BTO NPs. (D) HRTEM image of t-BTO NPs and corresponding SAED pattern showing in the inset. (E) EDX surface-scan element distribution of Ba, Ti and O of t-BTO NPs. (F) Raman spectra of t-BTO NPs. (G, H) Height, piezoelectric amplitude and phase images of t-BTO NPs (G) and c-BTO NPs (H). (I, J) Amplitude loop curve and phase loop curve of c-BTO NPs (I) and t-BTO NPs (J) at an ac voltage from −4 V to 4 V. (K) The polarization-electric field (P–E) hysteresis curves of c-BTO NPs and t-BTO NPs. (L) COMSOL simulation of the piezopotential generated by one single t-BTO NP under varied US intensities. Inset displays the piezopotential distribution under 2 W cm^{-2} US stimulation.

(Fig. 1A), while c-BTO NPs exhibited a single characteristic peak at the same position (Fig. S1). From the scanning electron microscopy (SEM) (Fig. 1B, inset), transmission electron microscope (TEM) image (Fig. 1C), and selected area electron diffraction (SAED, Fig. 1D, inset) results, t-BTO NPs had nearly cubic morphology with a uniform size distribution of 148.75 ± 4.2 nm, with interplanar spacing distances of 0.402 nm and 0.398 nm representing (001) and (100) planes of BTO, respectively [42]. In comparison, c-BTO NPs presented similar morphology with an average size of 136.9 nm (Fig. S2). The energy-dispersive X-ray (EDX) mapping indicated homogeneous distribution of Ba, Ti, and O elements with an atomic ratio of 1:1:3 (Fig. 1E, Fig. S3). The two nanoparticles showed no significant difference in zeta potential (Fig. S4). The B1+E (307 cm^{-1}) scattering mode in the Raman spectrum was from the asymmetric vibration of the [TiO_6] octahedra (Fig. 1F) [35,43], also verifying the noncentrosymmetric structure and tetragonal distortion.

Piezoelectric force microscopy (PFM) results confirmed the piezoelectric responsive capacity of t-BTO NPs (Fig. 1G and H). In the amplitude and phase maps under the applied voltage bias, the bright and dark regions were well-matched, confirming piezoelectricity (Fig. 1G). The butterfly-shape amplitude curve and the diamond-shaped 180° hysteresis loop indicated the local polarization switching under the voltage bias, which showed no obvious response change for the c-BTO NPs (Fig. 1I). The presence of ferroelectric hysteresis suggested t-BTO NPs had the capability of the electromechanical conversion (Fig. 1J). The P-E measurement result also confirmed ferroelectricity (Fig. 1K). The remnant polarization of t-BTO NPs was 4.98 μC/cm, displaying an optimized dipole orientation relative to c-BTO NPs. We simulated the piezoresponse of a single t-BTO NP under US irradiation via finite element modeling (FEM). Piezopotential at the surface of t-BTO NP gradually increased with the elevated US power intensities (0.5, 1, 1.5, and 2 W cm^{-2}; 1 MHz) and reached 45.4 mV at 2 W cm^{-2} US irradiation (Fig. 1L, Fig. S5). All these results confirmed the excellent piezoelectricity of t-BTO NPs.

Next, we confirmed that MA had been grafted to the hydrogel using ^{1}H NMR showing an increase in signal at δ = 5.3 and 5.5 ppm (the protons of methacrylatevinyl group of MA) (Fig. S6). SEM and EDX-mapping analyses verified successful incorporation of t-BTO NPs into the GelMA hydrogel (GelMA + t-BTO hydrogel) with micron-scale porous structure (Fig. 2A, Fig. S7), but our results also showed that BTO NPs existed in an agglomerated state in the hydrogels (Fig. 2A), suggesting that the uniform distribution of BTO NPs in hydrogels may need to be considered in future work. The compressive strength of the GelMA + c-BTO and GelMA + t-BTO hydrogels fell within the range of 20–45 kPa, while their corresponding elastic modulus was 10.15 ± 3.41 KPa and 14.85 ± 4.85 kPa, respectively (Fig. 2B and C), suitable for osteogenic differentiation of stem cells [44]. ICP-MS data further revealed a significant increase in barium and titanium content in the extracts of the piezoelectric GelMA + t-BTO group after 7, 14, 28 and 56 days of immersion in PBS (Fig. S8), indicating gradual release of t-BTO NPs into the local microenvironment to perform various biological functions. We confirmed the piezoelectricity of the piezoelectric hydrogel by detecting the mechanical-electric response of the assembled piezoelectric generator device under various forces (Fig. 2D). Fig. 2E showed no obvious electric signal detected in the device from the pure GelMA hydrogels. For the GelMA + t-BTO hydrogel assembled generator, the open-circuit voltage (V_{oc}) was approximately 52 mV under a periodically constant force of 200 kPa, which was 3.8-fold higher than

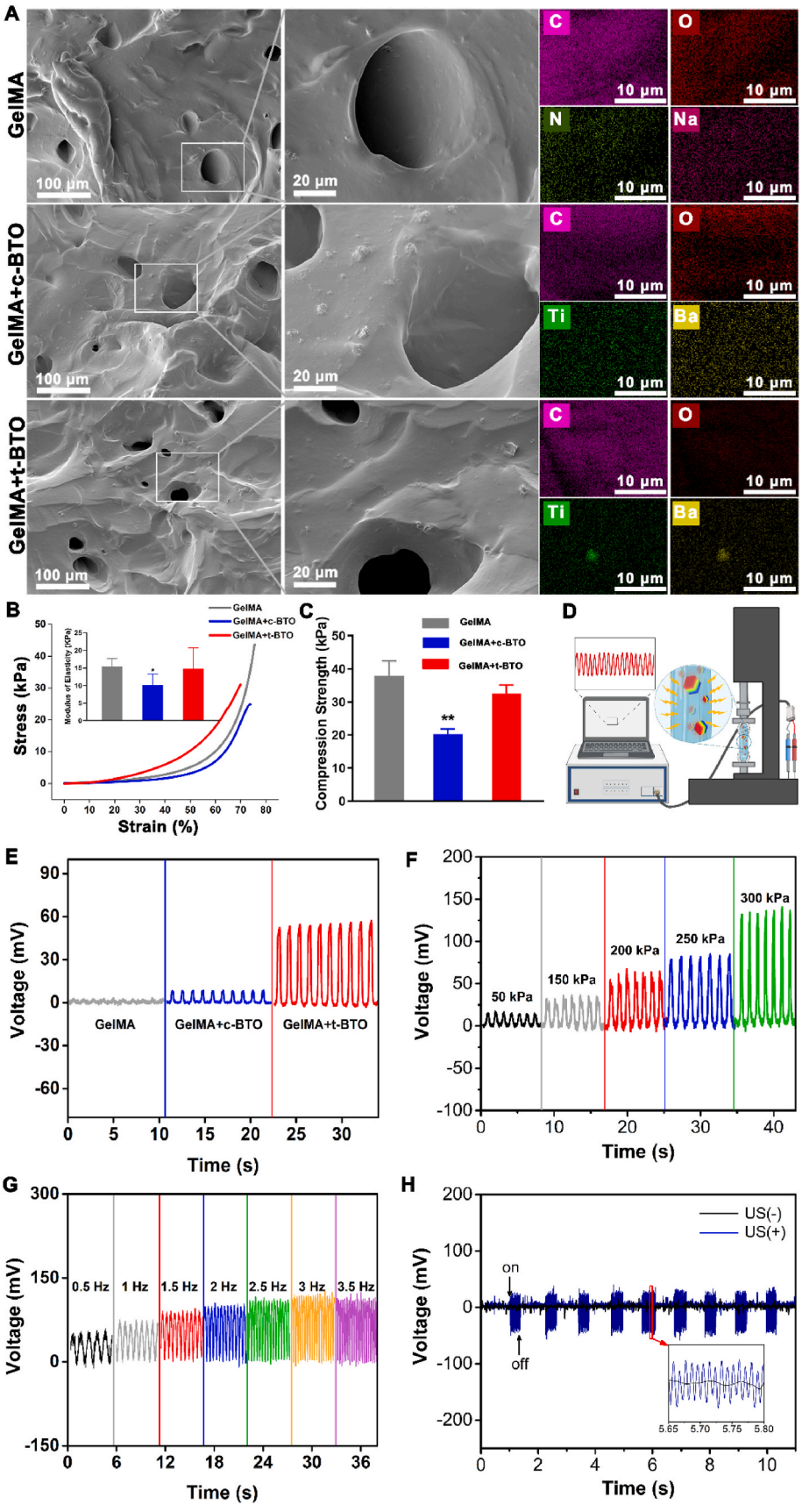

(caption on next page)

Fig. 2. Characterization of piezoelectric properties of piezoelectric hydrogels. (A) SEM images and EDX surface-scan element distribution of GelMA, GelMA + c-BTO, and GelMA + t-BTO. (B) Compressive stress-strain curves (the inserted picture represents elastic modulus) and (C) compression strength of GelMA, GelMA + c-BTO, and GelMA + t-BTO. (D) Schematic diagram of the piezoelectric performance test system for the piezoelectric hydrogels. (E) Open-circuit voltages of generator devices made from various hydrogels under a force of 200 kPa. (F) Open-circuit voltages of devices made from GelMA + t-BTO hydrogel under variable forces from 50 to 300 kPa. (G) Open-circuit voltages of device made from GelMA + t-BTO hydrogel under constant force within the frequency range of 0.5–3.5 Hz. (H) Mechanical-electric response of GelMA + t-BTO hydrogel before and after ultrasound stimulation.

that from the GelMA + c-BTO hydrogel. Furthermore, we detected V_{oc} of the generator from the GelMA + t-BTO hydrogel under 50–300 kPa and 0.5–3.5 Hz, which was close to the stress transferred to the periodontal tissue and the frequencies of chewing motion, respectively (Fig. 2F and G) [45]. As shown in Fig. 2G, the electric output was 32.7 mV at 0.5 Hz and increased to 113 mV when the frequency reached 2.5 Hz. Notably, the voltage value remained unchanged when the frequency value was over 2.5 Hz, attributed to the deformation relaxation of the hydrogel. Besides, the device from the GelMA + t-BTO hydrogel output 40 mV voltage when exposed to the ultrasound stimulation, demonstrating that the GelMA-based hydrogel possessed high electromechanical response sensitivity (Fig. 2H). These results confirmed that the GelMA + t-BTO hydrogel can effectively generate electric signals for piezoelectric stimulation under various external forces, encouraging us to use it as a wireless nanotransducer to impose dynamically-tunable piezoelectric stimulation.

3.2. Wireless piezoelectric stimulation enhanced mitochondrial bioenergetics to rescue impaired osteogenesis

We evaluated whether the piezoelectric stimulation can rescue impaired osteogenic capability in inflammatory PDLSCs. To create an inflammation model, PDLSCs were treated with periodontal pathogen-derived lipopolysaccharide (Pg-LPS) [46], resulting in inflammatory PDLSCs denoted as L-PDLSCs. After incubation of t-BTO NPs, L-PDLSCs were subjected to US irradiation to generate piezoelectricity (Fig. 3A). Initially, the safe parameter for US (0.6 W cm^{-2}, 1 MHz, 60 s, 50% duty cycle) and dosage (50 μg mL^{-1}) of t-BTO NPs were determined, under which condition PDLSCs showed high viability and proliferation rates (Figs. S9 and S10). As shown in Fig. 3B, the decreased intracellular ATP level in L-PDLSCs was significantly restored to normal levels after treatment with t-BTO US^{+}. In contrast, this phenomenon was not observed in L-PDLSCs treated with t-BTO or c-BTO US^{+}. Additionally, t-BTO US^{+} treatment also remarkably elevated the mitochondrial membrane potential ($\Delta\psi_m$) in L-PDLSCs (Fig. 3C and D).

Adequate energy supply is an important determining factor for the osteogenic differentiation of stem cells, which involves collagen biosynthesis, as well as bone matrix protein and mineral deposition [14, 47]. We assessed the influence of piezoelectric stimulation on the osteogenic differentiation capacity of L-PDLSCs since it has the ability to elevate cellular ATP levels. The results of real-time quantitative polymerase chain reaction (qRT-PCR) revealed that after 5 days of t-BTO US^{+} treatment, the mRNA levels of two early osteogenic markers, alkaline phosphatase (ALP) and Runt-related transcription factor 2 (RunX2), were upregulated by 6-fold and 2-fold for L-PDLSCs, respectively (Fig. 3E and F). In contrast, neither c-BTO US^{+} nor t-BTO US^{-} treatment showed any effect on these osteogenic differentiation-related genes. Additionally, on day 14, the ALP expression in all groups reflected a similar trend of change (Fig. 3G, g). Moreover, extracellular matrix (ECM) mineralization as a late marker of osteogenic differentiation was also significantly enhanced for the cells after 21 days of t-BTO US^{+} treatment (Fig. 3H, h). These results suggested that t-BTO NPs under ultrasound stimulation can reverse the inflammatory state of PDLSCs and promote their osteogenic differentiation capacity.

3.3. Mechanism underlying piezoelectric stimulation-mediated bioenergetic activation and osteogenic differentiation

To investigate the potential mechanism underlying the bioenergetic activation and promotion of osteogenic differentiation, we used RNA sequencing (RNA-seq) to detect the complete transcriptional profile of L-PDLSCs after 5 days of t-BTO US^{+} stimulation. Heat map (Fig. 4A) and volcano plot (Fig. 4B) revealed a total of 1612 differentially expressed genes (DEGs) in the t-BTO US^{+} group relative to L-PDLSCs, among which 833 DEGs were up-regulated. Gene Ontology (GO) enrichment analysis displayed that the top 20 up-regulated clusters of biological processes included microtubule cytoskeleton organization involved in mitosis and microtubule cytoskeleton organization (Fig. 4D); the top 20 up-regulated clusters of cellular components included cytoskeleton, microtubule cytoskeleton, mitotic spindle, and microtubule organizing center (Fig. 4E); and the top 20 up-regulated clusters of molecular functions included ATPase activity (coupled), ATP binding, ATP dependent microtubule motor activity, microtubule binding and microtubule motor activity (Fig. 4F). We identified a significant positive correlation between energy utilization (ATPase activity) and microtubule cytoskeleton organization with a total of 147 highly interconnected genes (Fig. S11). Furthermore, the Kyoto Encyclopedia of Genes and Genomes (KEGG) pathway analysis showed that the upregulated DEGs were mostly enriched in phosphatidylinositol signaling (Fig. S12), inositol phosphate metabolism (Fig. S13), oxidative phosphorylation (OXPHOS, Fig. S14), and citrate cycle (TCA cycle, Fig. S15). Furthermore, t-BTO NPs were effective in down-regulating inflammation-related genes, including IL-1 β, IL-6, CCL2, SOD2, and tumor necrosis factor alpha-induced proteins (Fig. S16), suggesting that the piezoelectric effect reverses the inflammatory state and provides a prerequisite for osteogenesis in L-PDLSCs. All these results revealed that the piezoelectric stimulation can boost ATP generation in L-PDLSCs through OXPHOS and enhance energy utilization, which further drove downstream intracellular events including activation of phosphatidylinositol signaling system, cytoskeletal re-organization, and osteogenic differentiation.

As a dynamic network comprised of intermediate filaments, microfilaments, and microtubules, the cytoskeleton is involved in cell migration, adhesion, mitosis, and differentiation [48–50], during which phosphorylation of myosin light chain (MLC) is a key regulator. Phosphorylation of MLC also relies on the activity of Ca^{2+}-mediated myosin light chain kinase (MLCK), which activates ATPase of myosin and translocates actin filaments powered by ATP hydrolysis energy, resulting in their contraction and reorganization [48–50]. Therefore, we hypothesized that adequate ATP supply and specific intracellular Ca^{2+} activity may be prerequisites for cytoskeletal reorganization during osteogenic differentiation of PDLSCs. To verify this hypothesis, phosphorylated myosin light chain (*p*-MLC) was detected. TEM observation combined with ICP analysis was employed to monitor and measure the uptake and endocytosis rate of t-BTO NPs by L-PDLSCs. Our results indicated that both c-BTO and t-BTO NPs were localized in the cytoplasm of L-PDLSCs in the presence or absence of ultrasonication (Fig. 5A). It was of interest that the ICP results showed that t-BTO NPs were phagocytosed by L-PDLSC at a range from 5.08% to 10.97%, which was significantly higher than that of the c-BTO group (0.84%–2.10%) (Fig. S17). Immunofluorescence staining results (Fig. 5B–C, Fig. S18) showed that t-BTO US^{+} treatment of L-PDLSCs significantly upregulated *p*-MLC expression, and the *p*-MLC fibrillary networks stretched along the

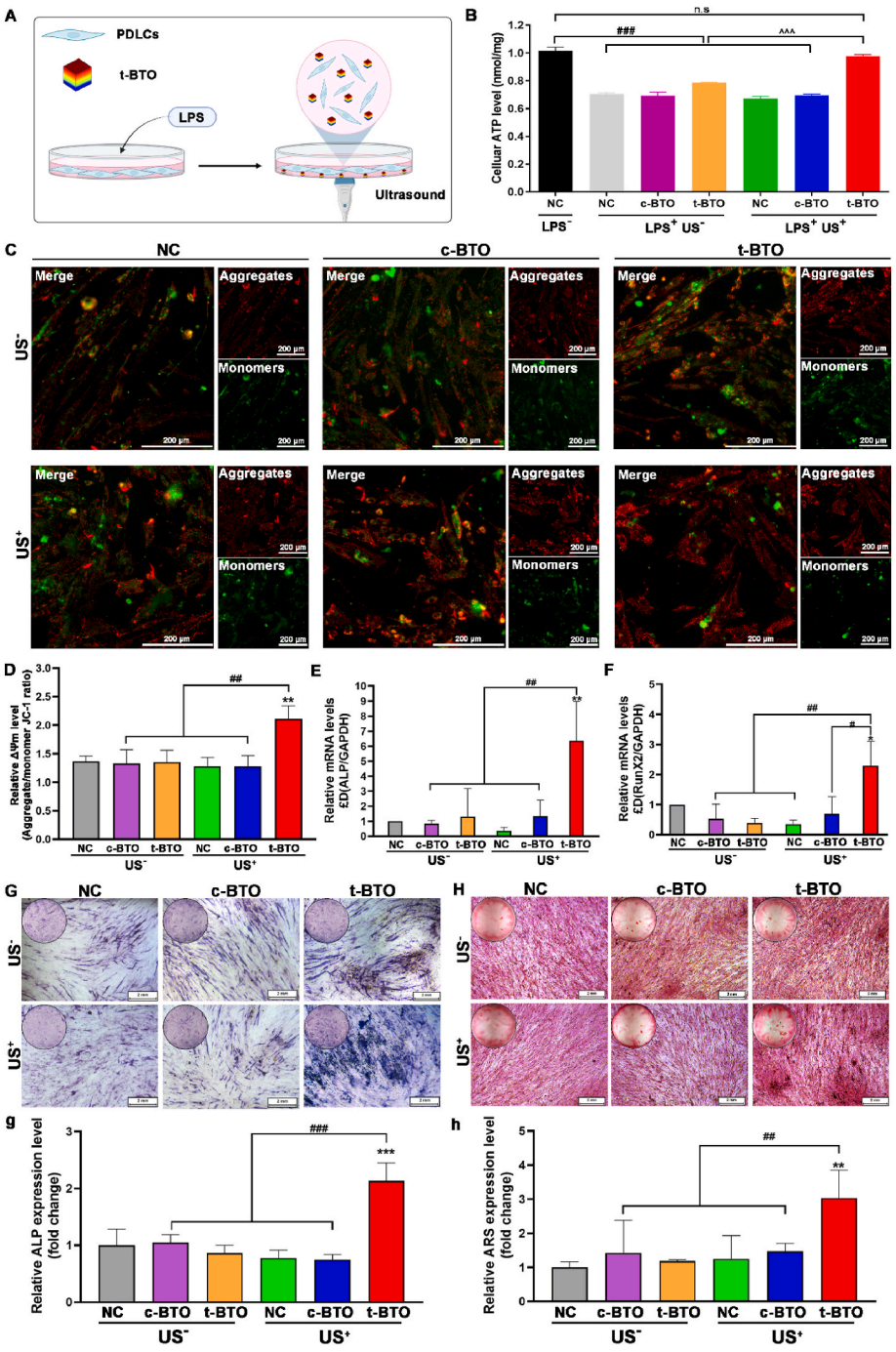

Fig. 3. Piezoelectric stimulation influences ATP levels, mitochondria membrane potential (ΔΨm), osteogenic differentiation-related gene expression, and mineralization in L-PDLSCs. (A) Schematic diagram of cellular experiment design. (B) Cellular ATP level of L-PDLSCs after various treatments for 3 days. n. s. $p > 0.05$, $^{###}p < 0.001$ vs. negative control (NC) without LPS (LPS^-). $^{\wedge\wedge\wedge}p < 0.001$ significant differences between groups under LPS stimulation. (C) Representative $\Delta\Psi_m$ fluorescence image and (D) quantitative analysis of the ratio of aggregates/monomers fluorescent intensity of L-PDLSCs after various treatments. $^{**}p < 0.01$ vs. NC US^- group. $^{\#\#}p < 0.01$ significant differences between groups. (E, F) Osteogenic differentiation-related gene ALP (E) and RunX2 (F) expression of L-PDLSCs after various treatments for 5 days. $^{*}p < 0.05$, $^{**}p < 0.01$ vs. NC US^- group. $^{\#}p < 0.05$, $^{\#\#}p < 0.01$ significant differences between groups. (G) Osteogenic mineralization-related ALP staining of L-PDLSCs after various treatments for 14 days, and (g) the relative ALP level in all groups. (H) Osteogenic mineralization-related ARS staining of L-PDLSCs after various treatments for 21 days, and (h) the relative ARS level in all groups. (NC US^-: negative control without ultrasound; c-BTO US^-: cubic $BaTiO_3$ without ultrasound; t-BTO US^-: tetragonal $BaTiO_3$ without ultrasound; NC US^+: negative control with ultrasound; c-BTO US^+: cubic $BaTiO_3$ with ultrasound; t-BTO US^+: tetragonal $BaTiO_3$ with ultrasound).

cell long axis and spread throughout the cytoplasm. In contrast, *p*-MLC expression after other treatments showed no obvious change, and the fluorescence was predominantly located on the perimeter of the cells. Next, we monitored changes in intracellular Ca^{2+} concentration ($[Ca^{2+}]_i$) following piezoelectric stimulation. As shown in Fig. 5D, in the t-BTO US^+ group, $[Ca^{2+}]_i$ continuously elevated and reached its peak at 9 h, then gradually declined but remained higher than in the untreated L-PDLSCs. A sustained increase in $[Ca^{2+}]_i$ with elevated $\Delta\psi_m$ was previously reported in hematopoietic stem cells upon stress hematopoiesis to initiate cell division [51]. An increase in $[Ca^{2+}]_i$ was also found to be

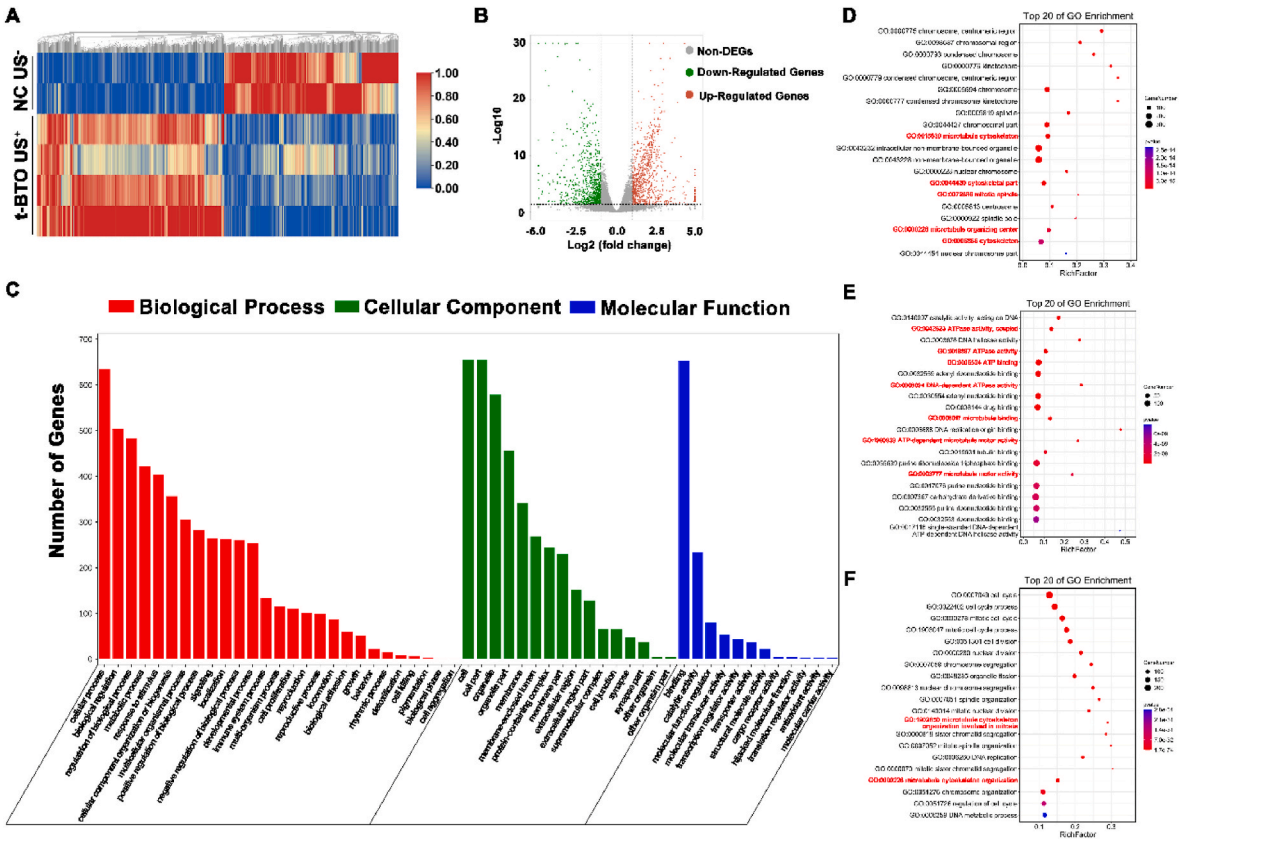

Fig. 4. Piezoelectric stimulation enhances ATPase activity and cytoskeleton organization-related gene clusters in the gene profile of L-PDLSCs. (A) Hierarchical cluster heatmap of differentially expressed genes (DEGs) in the NC US^{-} and the t-BTO US^{+} groups. Hierarchical cluster analysis was conducted for DEGs using a fold change <0.5 or >2 and $P < 0.05$. Red areas represent up-regulated DEGs, and blue areas represent down-regulated DEGs. (B) Volcano plot of DEGs in the NC US^{-} group and t-BTO US^{+} group. The detected genes are presented in the volcano plot using log 2 (fold change) as the x-axis and log 10 (P-value) as the y-axis. Red represents up-regulated DEGs, green represents down-regulated DEGs, and gray represents non-DEGs. (C) The differential genes were assigned to three GO categories: biological process, cellular component, and molecular function. (D, E, F) Top 20 bubble charts of the biological process (D), cellular component (E), and molecular function (F) of GO enrichment analysis for the up-regulated DEGs in the t-BTO US^{+} group. Low q-values are in red and high q-values are in blue; the size of the circle was proportional to the number of enriched genes.

capable of restoring the proliferative potential and rescuing age-induced loss of MSC function [52]. The positive feedback between $[Ca^{2+}]_i$ elevation and ATP production from mitochondria can satisfy the increased energetic demand in various cell behaviors [53]. Furthermore, it was found that phosphoinositide/Ca^{2+} signaling plays a key role in neuroprotection for impaired neuronal or aged astrocytes [53,54]. Collectively, combining these results with that fact that piezoelectric stimulation upregulated phosphatidylinositol signaling and OXPHOS, we deduced that piezoelectric stimulation can drive intracellular ATP synthesis by elevating $\Delta\psi_m$ via piezoelectric potential-evoked electron transfer. The resultant continuous rise in $[Ca^{2+}]_i$ and ATP with bidirectional positive feedback ultimately led to cytoskeleton reorganization and subsequent osteogenic differentiation mediated via phosphorylation of MLC using the chemical energy released from ATP hydrolysis (Fig. 5E).

3.4. Wireless piezoelectric stimulation rebuilt regenerative immune microenvironment

In addition to osteogenic differentiation, reconstructing a local pro-regenerative niche is essential for bone regeneration in periodontitis. We then evaluated whether piezoelectric stimulation can induce M2 polarization of macrophage to assist regeneration (Fig. 6A). As shown in Fig. 6B, LPS treatment caused originally sphere-shaped RAW 264.7 cells to become flattened with many extended pseudopodia (denoted as L-RAW 264.7 cells), displaying the typical morphological feature of M1 macrophages [55]. The t-BTO US^{+} treatment caused the L-RAW 264.7 cells to show apparent elongation and F-actin filament extension (Fig. 6B and C). More importantly, t-BTO US^{+} treatment significantly upregulated expression of arginase 1 (Arg-1) as the specific biomarker of M2 macrophage. It did not obviously affect the expression of inducible nitric oxide synthase (iNOS) as specific M1 macrophage biomarker (Fig. 6D and E) [55]. In contrast, the sham treatments (t-BTO US^{-}, c-BTO US^{-}, or c-BTO US^{+}) had no such an obvious influence on their expression, confirming the capacity of piezoelectric stimulation for M2 polarization of the macrophages. We used RNA-seq to analyze DEGs of the treated L-RAW 264.7 cells. After piezoelectric stimulation, there were 728 down-regulated and 125 up-regulated DEGs compared to the L-RAW 264.7 cells (Fig. S19). The top 20 enriched molecular function mainly involved the cluster of transmembrane channels, including ion channels, ion-gated channels, substrate-specific channels, cation channels, and voltage-gated ion channels (Fig. 5H, Fig. S20).

3.5. In vivo treatment of periodontitis with the piezoelectric hydrogel

With the positive effects of piezoelectric stimulation on osteogenic differentiation and macrophage phenotype switching *in vitro*, we then explored the immunomodulatory and bone regenerative capacities of the piezoelectric hydrogel for treating periodontitis *in vivo*. A periodontitis-involved bone defect model was established in rats by surgically preparing alveolar bone defects (Fig. S21) and locally injecting Pg-LPS. The successfully modeled animals were randomly assigned

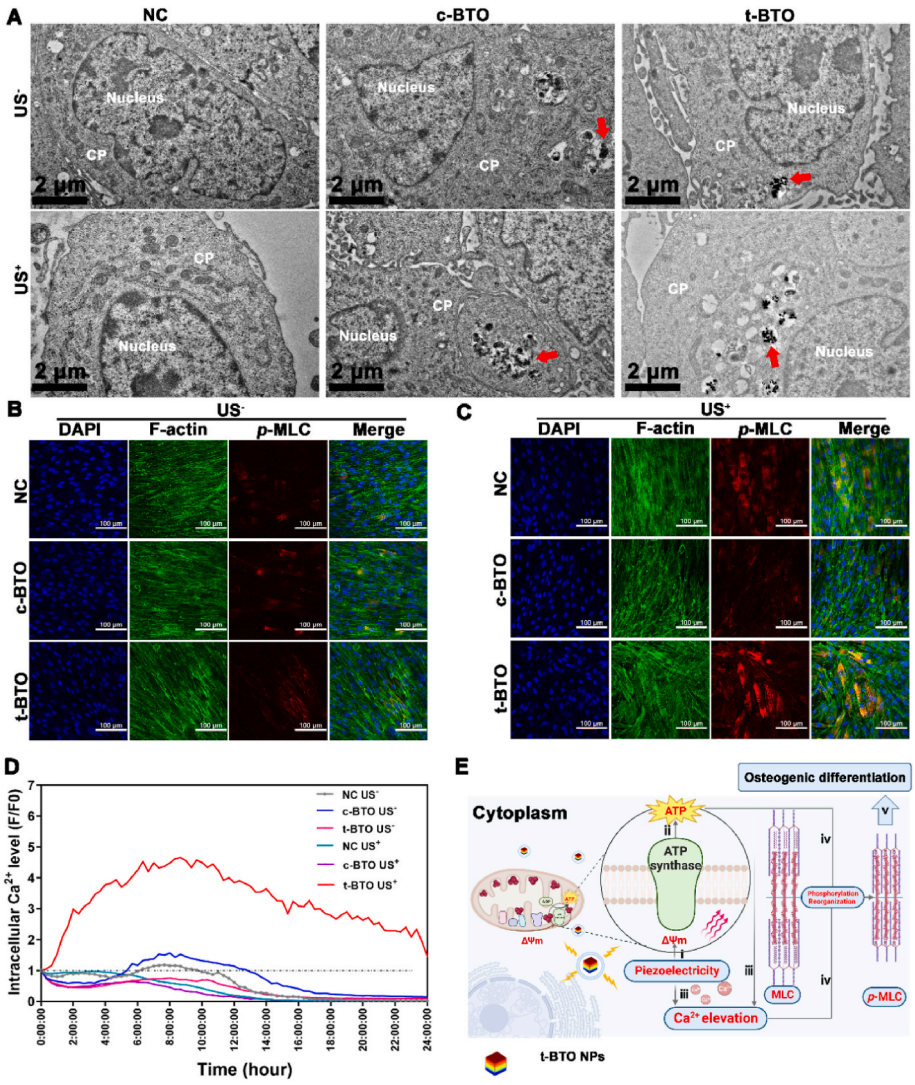

Fig. 5. Piezoelectric stimulation influences *p*-MLC expression and intercellular Ca^{2+} level in L-PDLSCs. (A) TEM images for intracellular localization of NPs. CP: Cytoplasm, Red arrow indicated NPs. (B, C) Representative *p*-MLC fluorescence image of L-PDLSCs exposed to the different groups at 3 days. (D) Intracellular Ca^{2+} level of L-PDLSCs after various treatments. (E) Mechanism schematic for the piezoelectric stimulation-mediated osteogenic differentiation of L-PDLSCs: i) piezoelectricity boosts $\Delta\psi_m$, ii) promotes intracellular ATP synthesis; iii) piezoelectricity and elevated ATP cause a rise in $[Ca^{2+}]_i$; iv) ATP hydrolysis and Ca^{2+} drive MLC phosphorylation mediating cell contraction and reorganization, and v) further osteogenic differentiation.

to four groups: i) Blank control, ii) GelMA hydrogel, iii) GelMA + c-BTO hydrogel, and iv) GelMA + t-BTO hydrogel (Fig. 7A). Surrounding the periodontal tissues, the piezoelectric hydrogel can generate piezoelectric stimulation under various physiological activities such as chewing. The micro-CT imaging results showed improved mineralization and reduced defect area after the GelMA + t-BTO treatment. After a chronic therapy for 12 weeks, the initial defect area was almost completely restored in the GelMA + t-BTO group (Fig. 7B). In contrast, after 12 weeks, limited bone tissue regeneration and more exposed tooth roots were observed in the other two GelMA-including groups (Group ii and Group iii), and the tooth root exposure was deteriorated in the blank control group due to the limited self-repairing capacity of bone tissue under the processive inflammatory microenvironment (Fig. 7B). Bone regeneration was further assessed through quantitative analyses of new bone volume (BV), bone volume/total volume (BV/TV), and bone mineral density (BMD) (Fig. 6C–E). After 4 weeks, BV/TV in the GelMA + t-BTO group (63.40 ± 5.58%) was significantly higher than the other two GelMA-including groups (40.85 ± 10.27% for the GelMA group and 40.37 ± 13.07% for the GelMA + c-BTO group, respectively) and the blank control group (44.15 ± 10.01%). At 12 weeks, compared to the blank control group, BV/TV in the other three GelMA groups were increased, and the GelMA + t-BTO group displayed the highest bone volume fraction (91.45 ± 5.68 %), an increase of 223.8%. An exciting increasing trend for BV and BMD was also observed in the GelMA + t-BTO group. In addition, the result of hematoxylin and eosin (H&E) staining of the bone regeneration area within the first molar root bifurcation area was consistent with the micro-CT imaging result (Fig. 7F and G). That is, the amount of newly regenerated bone tissue along the boundaries of the bone defect was significantly increased after 4 weeks and approximately occupied all the residual defect regions after 12 weeks in the GelMA + t-BTO group. By contrast, new bone formation at the defect areas in the other three groups was apparently insufficient, and in the blank control group, a considerable amount of fibrous connective tissue and more invasion of inflammatory cells were observed in the defect area (Fig. 7F and G).

The *in vitro* results revealed that piezoelectric stimulation can activate osteogenic differentiation of inflammatory PDLSCs via regulating the *p*-MLC-mediated cytoskeletal reorganization. Therefore, we detected *p*-MLC expression in the bifurcation region of the first molar root via immunohistochemistry staining. As shown in Fig. 7H, during the first 4

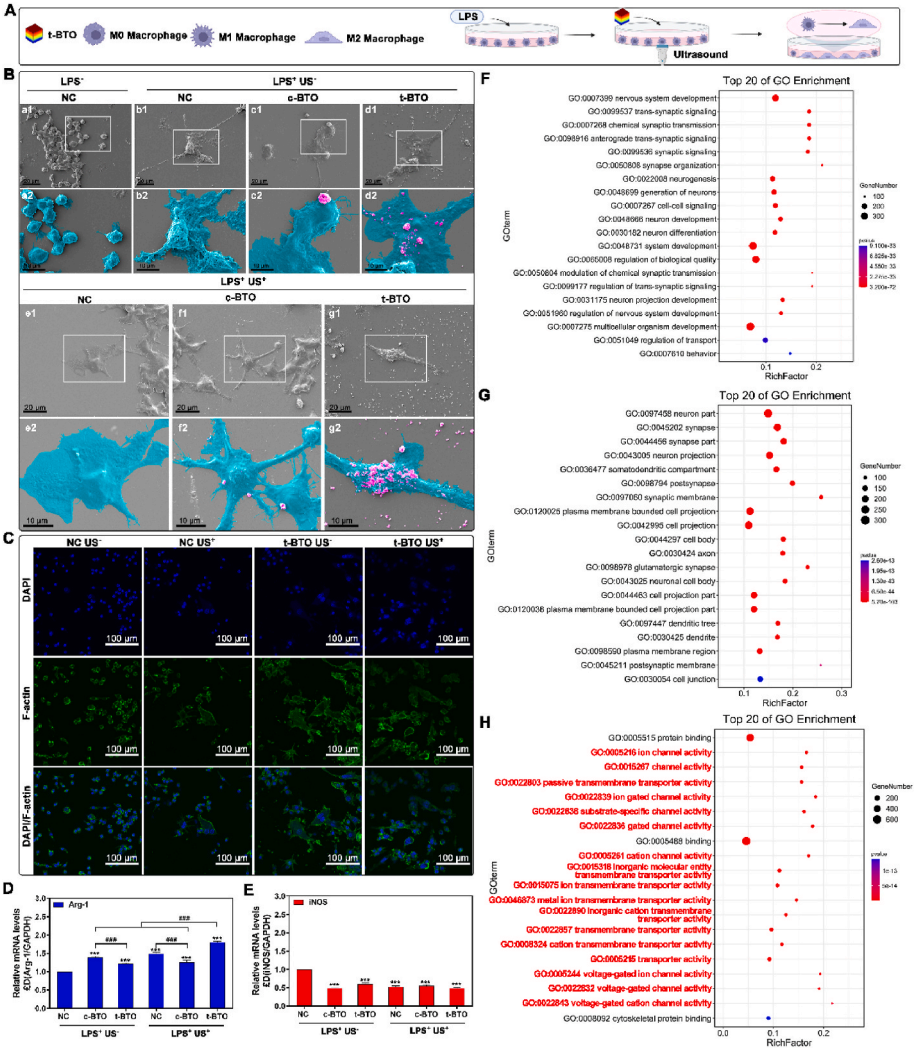

Fig. 6. Piezoelectric stimulation modulates M2 polarization of macrophages. (A) Schematic diagram of experimental design. (B) Representative SEM images of L-RAW 264.7 cells morphology cultured with different groups. (a2-g2): high magnification pseudo-colored micrographs of the white box area in (a1-g1). Tiffany blue represents L-RAW 264.7 cells, and peachy red represents nanoparticles. (C) Representative fluorescence image of L-RAW 264.7 cells after various treatments. (D, E) Phenotype-related gene Arg-1 (D) and iNOS (E) expression of L-RAW264.7 cells after various treatments. ***$p < 0.001$ vs. NC US$^-$. ###$p < 0.001$ significant differences between groups. (F–H) Top 20 bubble charts of the biological process (F), cellular component (G), and molecular function (H) of GO enrichment analysis in the NC US$^-$ group and t-BTO US$^+$ group. Low q-values are in red and high q-values are in blue; the size of the circle is proportional to the number of enriched genes.

weeks, *p*-MLC expression could be observed within the defect area in the GelMA + t-BTO group compared to the other three control groups, followed by downregulation of *p*-MLC expression after 12 weeks when newly formed bone had completely filled the defect area. These findings confirmed that the piezoelectric hydrogel can effectively rescue and accelerate osteogenesis in periodontitis.

We further examined whether the piezoelectric hydrogel can create a local pro-regenerative immune microenvironment by rebalancing the M1/M2 phenotype of macrophages. After 12 weeks of treatment, M1 macrophage phenotype (iNOS as the marker) and M2 macrophage phenotype (CD206 as the marker) in periodontal defects were analyzed via immunofluorescence staining. In the blank control group, a greater number of M1 macrophages were present in the defect area at 12 weeks. In the three GelMA hydrogel groups, especially the GelMA + t-BTO group, M1 macrophages were significantly decreased, and M2 macrophages were increased (Fig. 8A–C). Moreover, saliva from the rats was collected to analyze the levels of pro-inflammatory cytokines, including interleukin 1β (IL-1β), interleukin-6 (IL-6), and tumor necrosis factor alpha (TNF-α). As expected, local injection of Pg-LPS into periodontal defects induced a local inflammatory microenvironment with high levels of IL-1β, IL-6, and TNF-α (Fig. 8D). Following treatments, the concentrations of IL-1β, IL-6, and TNF-α in the three GelMA hydrogel treatment groups all decreased, with the GelMA + t-BTO piezoelectric hydrogel producing the most pronounced effects (Fig. 8D).

To distinguish the immunomodulatory role of piezoelectric stimulation from that of tilapia gelatin [32], we further detected the gene expression of M1 and M2 phenotype markers in L-RAW 264.7 after treatment with GelMA, GelMA + c-BTO, and GelMA + t-BTO. The results confirmed that all the non-piezoelectric and piezoelectric hydrogels can downregulate the gene expression of iNOS, while the piezoelectric hydrogel resulted in the highest expression of the M2 macrophage marker Arg-1 (Fig. S22). This demonstrated that the piezoelectric stimulation and the intrinsic anti-inflammatory activity of tilapia fish gelatin had a combination effect.

Last but not least, the biocompatibility of the piezoelectric hydrogel was assessed through hematological analysis, blood biochemical analysis, and histopathological analysis of the major organs after treatment. In all the groups, no evident injury or inflammatory lesions were identified in the major organs, including heart, lung, liver, spleen, and kidney, after 4 and 12 weeks of treatments (Fig. 8E and F). The

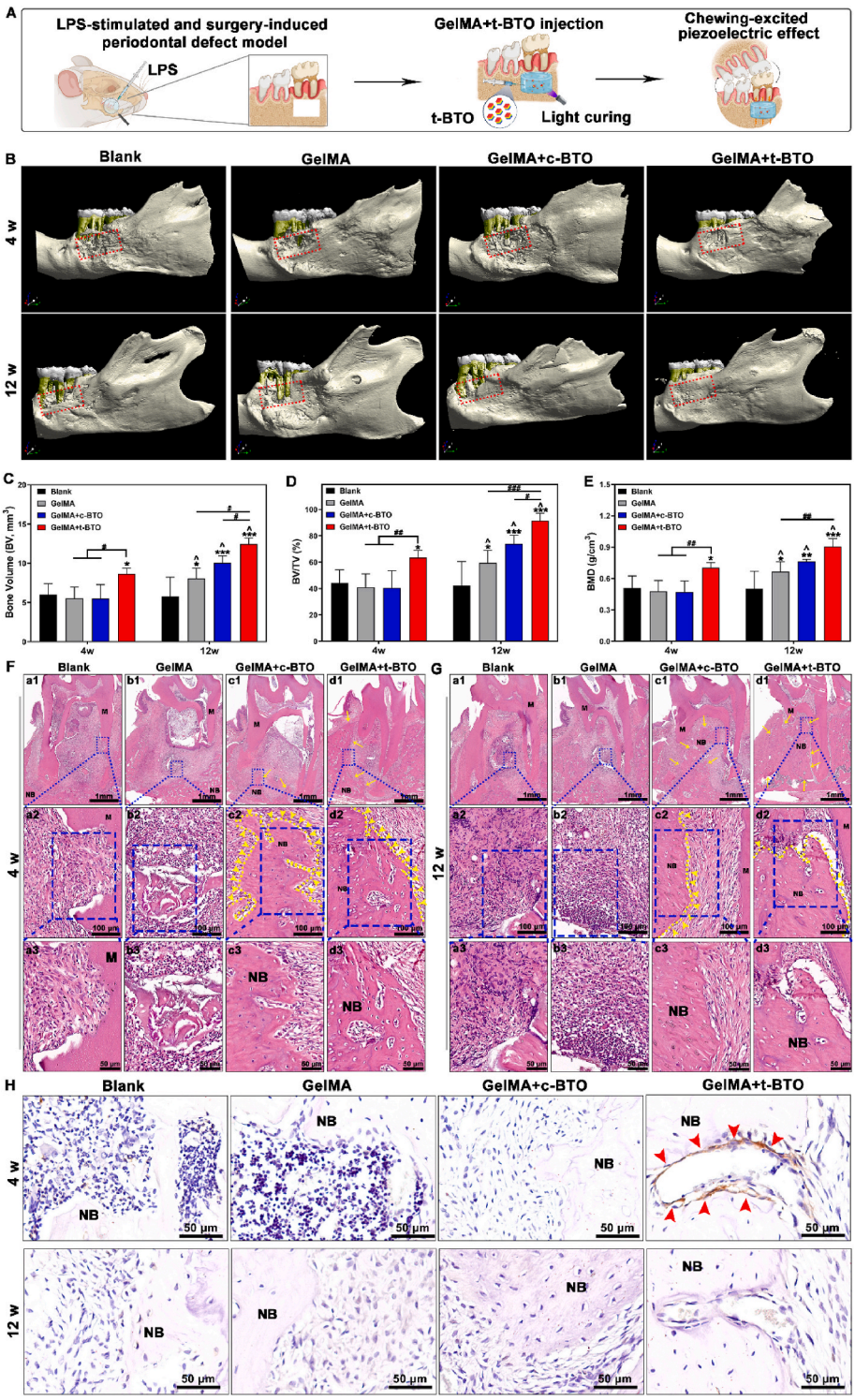

Fig. 7. Piezoelectric hydrogel promotes bone regeneration in periodontitis-periodontal defects. (A) Schematic diagram of the LPS and surgery-induced periodontitis defect model and treatment with the piezoelectric hydrogel. (B) Representative Micro-CT 3D construction images of bone repair after 4 weeks and 12 weeks post-surgery in the Blank group, GelMA group, GelMA + c-BTO group, and GelMA + t-BTO group. The red dotted frame denotes the defective area. (C) New bone volume (BV) analysis of the four groups at 4 weeks and 12 weeks. (D) Bone volume/total volume fraction (BV/TV) analysis of four groups at 4 w and 12 w. (E) Bone mineral density (BMD) analysis of the four groups at 4 weeks and 12 weeks. (F, G) H&E staining images of the four groups at 4 weeks (F) and 12 weeks (G). (a2-d2, 20 ×) Magnified images of the blue dashed region in (a1-d1, 2 ×), (a3-d3, 40 ×) Magnified images of the blue dashed region in (a2-d2, 40 ×). M: molar; NB: new bone. (H) Representative *p*-MLC immunohistochemistry images (80 ×) of the four groups at 4 weeks and 12 weeks. Red arrows point to the expressed *p*-MLC. *$p < 0.05$, **$p < 0.01$, ***$p < 0.001$ vs. Blank group at 4w and 12w. $^{\#}p < 0.05$, $^{\#\#}p < 0.01$, $^{\#\#\#}p < 0.001$ significant differences between groups. $^{\wedge}p < 0.05$ significant differences between 4 weeks and 12 weeks.

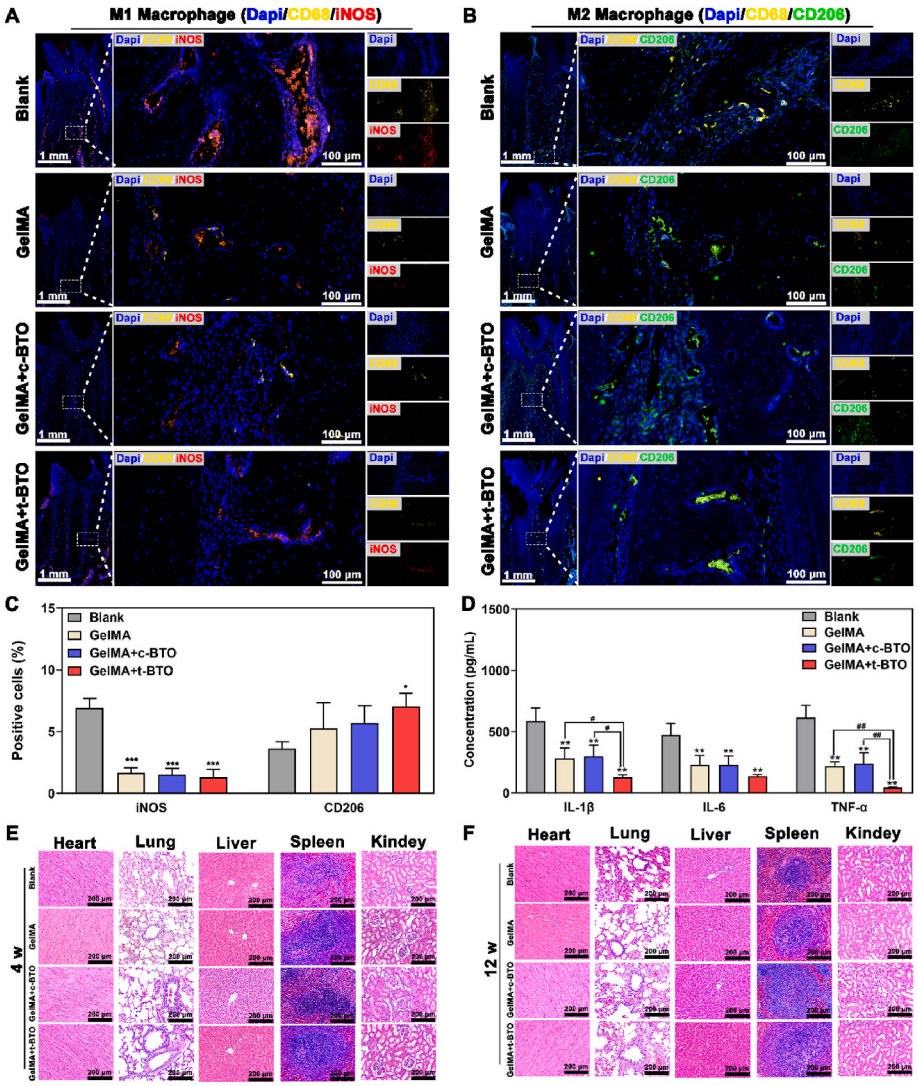

Fig. 8. Piezoelectric hydrogel exhibits no major organ damage and reduces inflammatory response by modulating M1/M2 macrophages in periodontitis-periodontal defects. (A–C) Representative fluorescence images and positive percentage of M1 and M2 macrophages in the defects of the four groups at 12 weeks. (D) Salivary inflammatory factors (IL-1β, IL-6, and TNF-α) after 12 weeks of post-surgery. (E, F) H&E staining images (10 ×) of major organs in the four groups at 4 weeks and 12 weeks. *p < 0.05, **p < 0.01 vs. Blank group. #p < 0.05, ##p < 0.01 significant differences between groups.

hematological and blood biochemical analyses showed no significant differences among the groups (Table S3 and Table S4). In addition, GelMA + t-BTO did not affect the expression of $CD4^+$ T cells and $CD8^+$ T cells, and more importantly, there was no significant difference in the $CD4^+/CD8^+$ ratios for each group (Fig. S23), suggesting that GelMA + t-BTO does not produce significant immune-activating or immune-suppressing effects on the organism. All these data indicate that piezoelectric hydrogels have favorable biocompatibility *in vivo*.

4. Discussion

Accumulated evidence suggests that mitochondrial dysfunction with deficient bioenergetics is a pivotal factor hampering tissue regeneration in chronic inflammatory diseases such as periodontitis, osteoarthritis, and neuroinflammation [6–9]. Researchers have found that electrical stimulation therapy in clinic can rescue inflammation-induced muscle mitochondrial dysfunction and accelerate tissue healing [19,56]. Among various modalities to deliver electrical stimulation, piezoelectric biomaterials stand out with their distinct advantages including non-invasiveness, wireless manipulation, high spatiotemporal precision, and tailorable biophysical cues [23–26]. This work provides new insights into the applications of piezoelectric biomaterials. We find that piezoelectric stimulation boosts mitochondrial bioenergetics, energizing impaired stem cells for osteogenic differentiation and directing immunomodulation for pro-regeneration. This offers new opportunities to regenerate injured bone tissues under inflammatory states.

Under healthy conditions, PDLSCs have osteogenic differentiation abilities and play a critical role in periodontal metabolism and remodeling [57]. However, when exposed to chronical inflammation in periodontitis, their pluripotency and differentiation potential undergo progressive loss due to mitochondrial dysfunction and energy deficiency [6–9]. Generally, injured cells suffer from OXPHOS arrest with distorted mitochondrial activity. Consequently, a reversible damage phase is accompanied by rapid ATP depletion and interrupted protein synthesis, ultimately leading to irreversible cell damage or death [58]. Therefore, restoring OXPHOS and intracellular ATP of injured PDLSCs in their initial injury phase is critical for rescuing impaired osteogenic differentiation.

Herein, we first construct a dynamically-tunable wireless piezoelectric stimulation system responsive to mechanical stimuli. The wireless piezoelectric stimulation successfully reverses mitochondrial dysfunction of L-PDLSCs, as evidenced by elevated $\Delta\psi_m$ and

intracellular ATP levels (Fig. 3B–D). Moreover, mitochondrial OXPHOS genes, phosphoinositide/Ca^{2+} signaling pathway and cytoskeletal re-organization related genes are significantly upregulated (Fig. 4, Figs. S12–S15). OXPHOS for ATP production is coupled to electron transport chain within the mitochondrial membrane [59]. So we deduce that the piezoelectric stimulation may elevate the intracellular ATP level via modulating the electron transport chain in mitochondria. Similarly, electromagnetic stimulation is reported to enhance OXPHOS by provoking mitochondrial complex I activity in electron transport chain, promoting the bone forming capacity of osteogenic cells [18]. In previous reports, a metabolic shift from glycolysis towards OXPHOS was found to be conducive to producing more ATP to meet the high energy demands for the osteogenic differentiation of mesenchymal stem cells [60]. Moreover, previous studies, including ours, have consistently reported that piezoelectric biomaterials can modulate cell spreading and cytoskeleton re-organization to control stem cell differentiation [23,25]. Recent studies have suggested that enhanced actomyosin cytoskeleton contractility and increased *p*-MLC expression are critical for osteogenesis [48,61]. Our results demonstrate that piezoelectric stimulation induces osteogenic differentiation of inflammatory PDLSCs (Fig. 3E–H). Interestingly, we find that cytoskeleton re-organization is accompanied by an upregulation of *p*-MLC and $[Ca^{2+}]_i$ increase after the piezoelectric stimulation, highly correlated with the recovery of mitochondrial bioenergetics and osteogenic differentiation potential (Figs. 3–5, Fig. S18).

Consistent with the *in vitro* results, in situ high-quality bone regeneration is also achieved in an inflammatory periodontal defect model in rats. At the early stage of bone healing *in vivo*, *p*-MLC expression significantly increases in the defects, confirming that wireless piezoelectric stimulation activates cytoskeleton re-organization (Fig. 7). Taken together, our findings suggest that wireless piezoelectric stimulation may be a promising approach to modulate energy metabolism for rescuing the impaired osteogenic differentiation of stem cells.

Severe periodontitis involves chronic inflammation with excessive M1 macrophage phenotype [62]. The prolonged and excessive M1 macrophage residence will lead to chronic inflammation, fibrous encapsulation, and delayed tissue healing [63,64]. In contrast, M2 macrophage can create a regeneration-favorable microenvironment by secreting anti-inflammatory/pro-repair factors [65]. Previous studies have found that electrical stimulation can inhibit ATP-sensitive potassium channels (K_{ATP} channel) to enhance macrophage M2 polarization [19,66]. Similarly, our findings show that piezoelectric stimulation, as a biophysical cue, can induce a direct phenotypic switch from M1 to M2 macrophages, which is highly related to ion channel modulation (Fig. 6, Fig. S20). To better create a local anti-inflammatory and pro-regenerative immune microenvironment, we incorporated t-BTO NPs into GelMA hydrogel with intrinsic anti-inflammatory activity to fabricate the piezoelectric hydrogel [32]. As a result, the piezoelectric hydrogel induces a phenotypic shift from M1 to M2 macrophages, shaping up a favorable anti-inflammatory and pro-regenerative niche (Figs. 6 and 8, and Fig. S22).

Overall, our findings pave a new way for the treatment of periodontitis through piezoelectric stimulation-enabled energy metabolism modulation and immunomodulation. However, there are several limitations and challenges that could be addressed in future research. First, to better reflect the interaction between oral bacteria and host responses involved in chronic periodontitis, the animal models by combination of microorganisms inoculations and surgical defect should be considered. Second, the mechanistic explanations of the piezoelectric-stimulated bioenergetics are highly relying on RNA-seq analysis. Further experimental validation of the proposed mechanisms is needed to establish causal relationships. Third, local injection of piezoelectric hydrogels into periodontal defects may result in the entire periodontal microenvironment being stimulated, which may lead to unknown effects. Therefore, we will switch our focus toward the effects of piezoelectric stimulation on other immune cell types such as neutrophil, dendritic cells or T lymphocytes. Finally, the piezoelectric hydrogels still face clinical translational challenges including unconsolidated *in vitro-in vivo* correlations, insufficient pre-clinical research data and a lack of unified guidelines for biological evaluation.

5. Conclusions

In summary, we developed a biocompatible piezoelectric hydrogel made from tilapia derived GelMA hydrogels and t-BTO NPs for treatment of periodontitis via modulating immunomodulation and osteogenesis. Piezoelectric stimulation-initiated ATP synthesis of inflammatory PDLSCs by elevating $\Delta\psi_m$, driving downstream energy-consuming events, including cytoskeletal re-organization and osteogenic differentiation. Furthermore, the piezoelectric hydrogel exhibited suitable immunomodulatory and excellent osteogenic capacity. In the inflammatory periodontal bone defects of rats, with the synergy of tilapia gelatin and piezoelectric stimulation, the piezoelectric hydrogel can shape up an anti-inflammatory and pro-regenerative niche by phenotypic switching from M1 to M2 macrophages, rescuing osteogenesis, and dramatically enhancing in situ bone regeneration. These findings validate that piezoelectric stimulation enabled energy metabolism and immunomodulation can rescue the impaired differentiation of stem cells in inflammatory microenvironments for bone regeneration.

Ethics approval and consent to participate

All animal studies were performed according to the guidelines set by the Independent Ethics Committee of Shanghai Ninth People's Hospital, Shanghai Jiao Tong University School of Medicine, and the overall project protocols were approved by The Independent Ethics Committee of Shanghai Ninth People's Hospital, Shanghai Jiao Tong University School of Medicine (SH9H-2022-A417-SB).

CRediT authorship contribution statement

Xin Liu: Writing – review & editing, Writing – original draft, Supervision, Conceptualization. **Xingyi Wan:** Writing – review & editing, Writing – original draft, Visualization, Methodology, Investigation. **Baiyan Sui:** Writing – review & editing, Writing – original draft, Visualization, Methodology, Investigation. **Quanhong Hu:** Writing – review & editing, Methodology, Investigation. **Zhirong Liu:** Writing – review & editing, Methodology, Investigation. **Tingting Ding:** Writing – review & editing, Methodology, Investigation. **Jiao Zhao:** Writing – review & editing, Visualization, Methodology, Investigation. **Yuxiao Chen:** Writing – review & editing, Methodology, Investigation. **Zhong Lin Wang:** Writing – review & editing, Supervision. **Linlin Li:** Writing – review & editing, Writing – original draft, Conceptualization.

Declaration of competing interest

The authors declare that they have no known competing financial interests or personal relationships that could have appeared to influence the work reported in this paper.

Acknowledgments

This work was sponsored by grants from the National Natural Science Foundation of China (82271024, 82072065, 82202333), National Clinical Key Specialty (Z155080000004), Science and Technology Commission of Shanghai Municipality (22DZ2201300), Shanghai Pujiang Programme (23PJD050), Innovative Research Team of High-level Local Universities in Shanghai (SHSMU-ZLCX20212400), Research Discipline fund (KQXJXK2023) from Ninth People's Hospital, Shanghai Jiao Tong University School of Medicine, and College of Stomatology, Shanghai Jiao Tong University, the Strategic Priority Research Program of the Chinese Academy of Sciences (No. XDA16021103), the Fundamental Research Funds for the Central

Universities (E2EG6802X2, E2E46801), and the National Youth Talent Support Program.

Appendix A. Supplementary data

Supplementary data to this article can be found online at https://doi.org/10.1016/j.bioactmat.2024.02.011.

References

[1] D.F. Kinane, P.G. Stathopoulou, P.N. Papapanou, Periodontal diseases, Nat. Rev. Dis. Prim. 3 (1) (2017) 1–14.

[2] G.A. Roth, D. Abate, K.H. Abate, S.M. Abay, C. Abbafati, N. Abbasi, H. Abbastabar, F. Abd-Allah, J. Abdela, A. Abdelalim, Global, regional, and national age-sex-specific mortality for 282 causes of death in 195 countries and territories, 1980–2017: a systematic analysis for the Global Burden of Disease Study 2017, Lancet 392 (10159) (2018) 1736–1788.

[3] G. Hajishengallis, T. Chavakis, Local and systemic mechanisms linking periodontal disease and inflammatory comorbidities, Nat. Rev. Immunol. 21 (7) (2021) 426–440.

[4] G. Hajishengallis, Periodontitis: from microbial immune subversion to systemic inflammation, Nat. Rev. Immunol. 15 (1) (2015) 30–44.

[5] P. Li, Q. Ou, S. Shi, C. Shao, Immunomodulatory properties of mesenchymal stem cells/dental stem cells and their therapeutic applications, Cell. Mol. Immunol. 20 (6) (2023) 558–569.

[6] Q. Zhai, X. Chen, D. Fei, X. Guo, X. He, W. Zhao, S. Shi, J.J. Gooding, F. Jin, Y. Jin, Nanorepairers rescue inflammation-induced mitochondrial dysfunction in mesenchymal stem cells, Adv. Sci. 9 (4) (2022) 2103839.

[7] P. Govindaraj, N.A. Khan, P. Gopalakrishna, R.V. Chandra, A. Vanniarajan, A. A. Reddy, S. Singh, R. Kumaresan, G. Srinivas, L. Singh, Mitochondrial dysfunction and genetic heterogeneity in chronic periodontitis, Mitochondrion 11 (3) (2011) 504–512.

[8] P. Bullon, H.N. Newman, M. Battino, Obesity, diabetes mellitus, atherosclerosis and chronic periodontitis: a shared pathology via oxidative stress and mitochondrial dysfunction? Periodontology 64 (1) (2000) 139–153, 2014.

[9] X. Li, B.-M. Tian, D.-K. Deng, F. Liu, H. Zhou, D.-Q. Kong, H.-L. Qu, L.-J. Sun, X.-T. He, F.-M. Chen, LncRNA GACAT2 binds with protein PKM1/2 to regulate cell mitochondrial function and cementogenesis in an inflammatory environment, Bone Res. 10 (1) (2022) 29.

[10] K. Ito, T. Suda, Metabolic requirements for the maintenance of self-renewing stem cells, Nat. Rev. Mol. Cell Biol. 15 (4) (2014) 243–256.

[11] S. Willenborg, D.E. Sanin, A. Jais, X. Ding, T. Ulas, J. Nuchel, M. Popovic, T. MacVicar, T. Langer, J.L. Schultze, A. Gerbaulet, A. Roers, E.J. Pearce, J. C. Bruning, A. Trifunovic, S.A. Eming, Mitochondrial metabolism coordinates stage-specific repair processes in macrophages during wound healing, Cell Metabol. 33 (12) (2021) 2398–2414 e9.

[12] S.A. Eming, T.A. Wynn, P. Martin, Inflammation and metabolism in tissue repair and regeneration, Science 356 (6342) (2017) 1026–1030.

[13] K. Ning, S. Liu, B. Yang, R. Wang, G. Man, D.E. Wang, H. Xu, Update on the effects of energy metabolism in bone marrow mesenchymal stem cells differentiation, Mol. Metabol. 58 (2022) 101450.

[14] H. Liu, Y. Du, J.P. St-Pierre, M.S. Bergholt, H. Autefage, J. Wang, M. Cai, G. Yang, M.M. Stevens, S. Zhang, Bioenergetic-active materials enhance tissue regeneration by modulating cellular metabolic state, Sci. Adv. 6 (13) (2020) eaay7608.

[15] C. Ma, M.L. Kuzma, X. Bai, J. Yang, Biomaterial-based metabolic regulation in regenerative engineering, Adv. Sci. 6 (19) (2019) 1900819.

[16] S. Lin, S. Yin, J. Shi, G. Yang, X. Wen, W. Zhang, M. Zhou, X. Jiang, Orchestration of energy metabolism and osteogenesis by Mg(2+) facilitates low-dose BMP-2-driven regeneration, Bioact. Mater. 18 (2022) 116–127.

[17] C. Ma, X. Tian, J.P. Kim, D. Xie, X. Ao, D. Shan, Q. Lin, M.R. Hudock, X. Bai, J. Yang, Citrate-based materials fuel human stem cells by metabonegenic regulation, Proc. Natl. Acad. Sci. U. S. A. 115 (50) (2018) E11741–E11750.

[18] A.M. Hollenberg, A. Huber, C.O. Smith, R.A. Eliseev, Electromagnetic stimulation increases mitochondrial function in osteogenic cells and promotes bone fracture repair, Sci. Rep. 11 (1) (2021) 19114.

[19] L. Leppik, K.M.C. Oliveira, M.B. Bhavsar, J.H. Barker, Electrical stimulation in bone tissue engineering treatments, Eur. J. Trauma Emerg. Surg. 46 (2) (2020) 231–244.

[20] K.M.C. Oliveira, J.H. Barker, E. Berezikov, L. Pindur, S. Kynigopoulos, M. Eischen-Loges, Z. Han, M.B. Bhavsar, D. Henrich, L. Leppik, Electrical stimulation shifts healing/scarring towards regeneration in a rat limb amputation model, Sci. Rep. 9 (1) (2019) 11433.

[21] M.B. Bhavsar, Z. Han, T. DeCoster, L. Leppik, K.M. Costa Oliveira, J.H. Barker, Electrical stimulation-based bone fracture treatment, if it works so well why do not more surgeons use it? Eur. J. Trauma Emerg. Surg. 46 (2) (2020) 245–264.

[22] C. Khatua, D. Bhattacharya, V.K. Balla, In situ electrical stimulation for enhanced bone growth: a mini-review, Med. Devices Sens. 3 (4) (2020) e10090.

[23] Z. Liu, M. Cai, X. Zhang, X. Yu, S. Wang, X. Wan, Z.L. Wang, L. Li, Cell-Traction-triggered on-demand electrical stimulation for neuron-like differentiation, Adv. Mater. 33 (51) (2021) e2106317.

[24] W. Liu, X. Li, Y. Jiao, C. Wu, S. Guo, X. Xiao, X. Wei, J. Wu, P. Gao, N. Wang, Y. Lu, Z. Tang, Q. Zhao, J. Zhang, Y. Tang, L. Shi, Z. Guo, Biological effects of a three-dimensionally printed Ti6Al4V scaffold coated with piezoelectric BaTiO(3) nanoparticles on bone formation, ACS Appl. Mater. Interfaces 12 (46) (2020) 51885–51903.

[25] X. Zhang, C. Zhang, Y. Lin, P. Hu, Y. Shen, K. Wang, S. Meng, Y. Chai, X. Dai, X. Liu, Y. Liu, X. Mo, C. Cao, S. Li, X. Deng, L. Chen, Nanocomposite membranes enhance bone regeneration through restoring physiological electric microenvironment, ACS Nano 10 (8) (2016) 7279–7286.

[26] S. Chen, P. Zhu, L. Mao, W. Wu, H. Lin, D. Xu, X. Lu, J. Shi, Piezocatalytic medicine: an emerging frontier using piezoelectric materials for biomedical applications, Adv. Mater. (2023) e2208256.

[27] L. Roldan, C. Montoya, V. Solanki, K.Q. Cai, M. Yang, S. Correa, S. Orrego, A novel injectable piezoelectric hydrogel for periodontal disease treatment, ACS Appl. Mater. Interfaces 15 (37) (2023) 43441–43454.

[28] Z. Liu, X. Wan, Z.L. Wang, L. Li, Electroactive biomaterials and systems for cell fate determination and tissue regeneration: design and applications, Adv. Mater. 33 (32) (2021) e2007429.

[29] Y. Kong, F. Liu, B. Ma, J. Duan, W. Yuan, Y. Sang, L. Han, S. Wang, H. Liu, Wireless localized electrical stimulation generated by an ultrasound-driven piezoelectric discharge regulates proinflammatory macrophage polarization, Adv. Sci. 8 (13) (2021) 2100962.

[30] M. Dai, B. Sui, Y. Xue, X. Liu, J. Sun, Cartilage repair in degenerative osteoarthritis mediated by squid type II collagen via immunomodulating activation of M2 macrophages, inhibiting apoptosis and hypertrophy of chondrocytes, Biomaterials 180 (2018) 91–103.

[31] M. Dai, B. Sui, Y. Hua, Y. Zhang, B. Bao, Q. Lin, X. Liu, L. Zhu, J. Sun, A well defect-suitable and high-strength biomimetic squid type II gelatin hydrogel promoted in situ costal cartilage regeneration via dynamic immunomodulation and direct induction manners, Biomaterials 240 (2020) 119841.

[32] X. Xu, B. Sui, X. Liu, J. Sun, A bioinspired and high-strengthed hydrogel for regeneration of perforated temporomandibular joint disc: construction and pleiotropic immunomodulatory effects, Bioact. Mater. 25 (2023) 701–715.

[33] H.W. Lee, S. Moon, C.H. Choi, D.K. Kim, Synthesis and size control of tetragonal barium titanate nanopowders by facile solvothermal method, J. Am. Ceram. Soc. 95 (8) (2012) 2429–2434.

[34] K. Elkhoury, M. Morsink, Y. Tahri, C. Kahn, F. Cleymand, S.R. Shin, E. Arab-Tehrany, L. Sanchez-Gonzalez, Synthesis and characterization of C2C12-laden gelatin methacryloyl (GelMA) from marine and mammalian sources, Int. J. Biol. Macromol. 183 (2021) 918–926.

[35] J. Wu, Q. Xu, E. Lin, B. Yuan, N. Qin, S.K. Thatikonda, D. Bao, Insights into the role of ferroelectric polarization in piezocatalysis of nanocrystalline BaTiO3, ACS Appl. Mater. Interfaces 10 (21) (2018) 17842–17849.

[36] D. Kim, B. Langmead, S.L. Salzberg, HISAT: a fast spliced aligner with low memory requirements, Nat. Methods 12 (4) (2015) 357–360.

[37] B. Langmead, S.L. Salzberg, Fast gapped-read alignment with Bowtie 2, Nat. Methods 9 (4) (2012) 357–359.

[38] C. Chen, H. Chen, Y. Zhang, H.R. Thomas, M.H. Frank, Y. He, R. Xia, TBtools: an integrative toolkit developed for interactive analyses of big biological data, Mol. Plant 13 (8) (2020) 1194–1202.

[39] F.Q. Shang, S.Y. Liu, L.G. Ming, R. Tian, F. Jin, Y. Ding, Y.J. Zhang, H.M. Zhang, Z. H. Deng, Y. Jin, Human umbilical cord MSCs as new cell sources for promoting periodontal regeneration in inflammatory periodontal defect, Theranostics 7 (18) (2017) 4370–4382.

[40] D.T. Lasisi, S.T. Shittu, C.C. Meludu, A.A. Salami, Differential effects of total and partial sleep deprivation on salivary factors in Wistar rats, Arch. Oral Biol. 73 (2017) 100–104.

[41] E.O. Carvalho, M.M. Fernandes, J. Padrao, A. Nicolau, J. Marques-Marchan, A. Asenjo, F.M. Gama, C. Ribeiro, S. Lanceros-Mendez, Tailoring bacteria response by piezoelectric stimulation, ACS Appl. Mater. Interfaces 11 (30) (2019) 27297–27305.

[42] J. Wu, N. Qin, D.H. Bao, Effective enhancement of piezocatalytic activity of BaTiO3 nanowires under ultrasonic vibration, Nano Energy 45 (2018) 44–51.

[43] C.K. Jeong, C. Baek, A.I. Kingon, K.I. Park, S.H. Kim, Lead-free perovskite nanowire-employed piezopolymer for highly efficient flexible nanocomposite energy harvester, Small 14 (19) (2018) 1704022.

[44] N. Huebsch, P.R. Arany, A.S. Mao, D. Shvartsman, O.A. Ali, S.A. Bencherif, J. Rivera-Feliciano, D.J. Mooney, Harnessing traction-mediated manipulation of the cell/matrix interface to control stem-cell fate, Nat. Mater. 9 (6) (2010) 518–526.

[45] M. Gupta, K. Madhok, R. Kulshrestha, S. Chain, H. Kaur, A. Yadav, Determination of stress distribution on periodontal ligament and alveolar bone by various tooth movements–A 3D FEM study, J. Oral Biol. Craniofacial Res. 10 (4) (2020) 758–763.

[46] Y. Zhang, X. Yuan, Y. Wu, M. Pei, M. Yang, X. Wu, Y. Pang, J. Wang, Liraglutide regulates bone destruction and exhibits anti-inflammatory effects in periodontitis in vitro and in vivo, J. Dent. 94 (2020) 103310.

[47] Q. Li, Z. Gao, Y. Chen, M.X. Guan, The role of mitochondria in osteogenic, adipogenic and chondrogenic differentiation of mesenchymal stem cells, Protein Cell 8 (6) (2017) 439–445.

[48] T. Yamamoto, Y. Ugawa, K. Yamashiro, M. Shimoe, K. Tomikawa, S. Hongo, S. Kochi, H. Ideguchi, H. Maeda, S. Takashiba, Osteogenic differentiation regulated by Rho-kinase in periodontal ligament cells, Differentiation 88 (2–3) (2014) 33–41.

[49] S.M. Naqvi, L.M. McNamara, Stem cell mechanobiology and the role of biomaterials in governing mechanotransduction and matrix production for tissue regeneration, Front. Bioeng. Biotechnol. 8 (2020) 597661.

[50] T. Kampourakis, Y.B. Sun, M. Irving, Myosin light chain phosphorylation enhances contraction of heart muscle via structural changes in both thick and thin filaments, Proc. Natl. Acad. Sci. U. S. A. 113 (21) (2016) E3039–E3047.

[51] T. Umemoto, M. Hashimoto, T. Matsumura, A. Nakamura-Ishizu, T. Suda, Ca(2+)-mitochondria axis drives cell division in hematopoietic stem cells, J. Exp. Med. 215 (8) (2018) 2097–2113.
[52] N. Ahamad, Y. Sun, B.B. Singh, Increasing cytosolic Ca(2+) levels restore cell proliferation and stem cell potency in aged MSCs, Stem Cell Res. 56 (2021) 102560.
[53] J.-P. Decuypere, G. Monaco, L. Missiaen, H. De Smedt, J.B. Parys, G. Bultynck, IP3 receptors, mitochondria, and Ca2+ signaling: implications for aging, J. Aging Res. 2011 (2011).
[54] J. Wu, J.D. Holstein, G. Upadhyay, D.-T. Lin, S. Conway, E. Muller, J.D. Lechleiter, Purinergic receptor-stimulated IP3-mediated Ca2+ release enhances neuroprotection by increasing astrocyte mitochondrial metabolism during aging, J. Neurosci. 27 (24) (2007) 6510–6520.
[55] F.Y. McWhorter, T. Wang, P. Nguyen, T. Chung, W.F. Liu, Modulation of macrophage phenotype by cell shape, Proc. Natl. Acad. Sci. U. S. A. 110 (43) (2013) 17253–17258.
[56] K. Tanaka, M. Tanaka, J. Takegaki, H. Fujino, Preventive effects of electrical stimulation on inflammation-induced muscle mitochondrial dysfunction, Acta Histochem. 118 (5) (2016) 464–470.
[57] Z. Khorolsuren, O. Lang, E. Pallinger, A. Foldes, G.G. Szabolcs, G. Varga, G. Mezo, J. Vag, L. Kohidai, Functional and cell surface characteristics of periodontal ligament cells (PDLCs) on RGD-synthetic polypeptide conjugate coatings, J. Periodontal. Res. 55 (5) (2020) 713–723.
[58] M.A. Miller, J.F. Zachary, Mechanisms and Morphology of Cellular Injury, Adaptation, and Death, Pathologic Basis of Veterinary Disease, 2017, p. 2.
[59] S. Liu, S. Liu, B. He, L. Li, L. Li, J. Wang, T. Cai, S. Chen, H. Jiang, OXPHOS deficiency activates global adaptation pathways to maintain mitochondrial membrane potential, EMBO Rep. 22 (4) (2021) e51606.
[60] E. Tsogtbaatar, C. Landin, K. Minter-Dykhouse, C.D.L. Folmes, Energy metabolism regulates stem cell pluripotency, Front. Cell Dev. Biol. 8 (2020) 87.
[61] K.A. Kilian, B. Bugarija, B.T. Lahn, M. Mrksich, Geometric cues for directing the differentiation of mesenchymal stem cells, Proc. Natl. Acad. Sci. U. S. A. 107 (11) (2010) 4872–4877.
[62] A. Almubarak, K.K.K. Tanagala, P.N. Papapanou, E. Lalla, F. Momen-Heravi, Disruption of monocyte and macrophage homeostasis in periodontitis, Front. Immunol. 11 (2020) 330.
[63] J. Stefanowski, A. Lang, A. Rauch, L. Aulich, M. Kohler, A.F. Fiedler, F. Buttgereit, K. Schmidt-Bleek, G.N. Duda, T. Gaber, R.A. Niesner, A.E. Hauser, Spatial distribution of macrophages during callus formation and maturation reveals close crosstalk between macrophages and newly forming vessels, Front. Immunol. 10 (2019) 2588.
[64] K. Zheng, W. Niu, B. Lei, A.R. Boccaccini, Immunomodulatory bioactive glasses for tissue regeneration, Acta Biomater. 133 (2021) 168–186.
[65] Z. Julier, A.J. Park, P.S. Briquez, M.M. Martino, Promoting tissue regeneration by modulating the immune system, Acta Biomater. 53 (2017) 13–28.
[66] C. Li, M. Levin, D.L. Kaplan, Bioelectric modulation of macrophage polarization, Sci. Rep. 6 (1) (2016) 21044.